

Imaging the three-dimensional orientation and rotational mobility of fluorescent emitters using the Tri-spot point spread function

Oumeng Zhang,¹ Jin Lu,¹ Tianben Ding,¹ and Matthew D. Lew¹

¹*Electrical & Systems Engineering, Washington University in St. Louis, St. Louis, Missouri, 63130, USA*

The fluorescence photons emitted by single molecules contain rich information regarding their rotational motions, but adapting single-molecule localization microscopy (SMLM) to measure their orientations and rotational mobilities with high precision remains a challenge. Inspired by dipole radiation patterns, we design and implement a Tri-spot point spread function (PSF) that measures the three-dimensional orientation and rotational mobility simultaneously of dipole-like emitters across a large field of view. We show that the orientation measurements using the Tri-spot PSF are sufficiently accurate to correct anisotropy-based localization bias, from 30 nm to 7 nm, in SMLM. We further characterize the emission anisotropy of fluorescent beads, revealing that both 20-nm and 100-nm diameter beads emit light significantly differently from isotropic point sources. Exciting 100-nm beads with linearly-polarized light, we observe significant depolarization of the emitted fluorescence using the Tri-spot PSF that is difficult to detect using other methods. Finally, we demonstrate that the Tri-spot PSF detects rotational dynamics of single molecules within a polymer thin film that are not observable by conventional SMLM.

Fluorescence microscopy has been widely used for imaging living cells due to the genetic specificity provided by tagging or protein engineering, its single-molecule (SM) sensitivity, and its minimal toxicity compared to other high-resolution imaging techniques. Super-resolution microscopy has recently broadened its capabilities, enabling images of dynamic living processes to be created with 1 nm spatial resolution¹⁻³ and 10 ms temporal resolution⁴. One class of super-resolution methods, termed single-molecule localization microscopy (SMLM), constructs high-resolution images by repeatedly measuring the positions of blinking molecules over time⁵⁻⁷. Beyond measuring molecular positions, SM imaging systems have also been augmented to measure molecular orientation^{8,9}, which is not only critical for ensuring the accuracy of SMLM^{8,10-12}, but is also helpful for elucidating a wide variety of biological processes¹³. By measuring molecular orientation and rotational mobility, researchers have gained insights into DNA bending and tangling^{9,14,15}, molecular motor dynamics¹⁶⁻¹⁸, and structures of polymer chains¹⁹⁻²¹.

Although the orientations of a molecule's absorption and emission dipole moments are not necessarily parallel²², optical methods are capable of measuring the orientations of both vectors. These techniques leverage 1) the absorption dipole moment's sensitivity to the polarization of the pumping light, 2) the polarization of the emitted fluorescence relative to the emission dipole moment, and/or 3) the dipole's anisotropic emission pattern. Since the probability of absorption is proportional to the square of the dot product between the absorption dipole moment and the local illuminating electric field, absorption-based methods

measure an emitter's fluorescence in response to varying the polarization of excitation light^{9,16,17}. Similarly, the orientation of an emission dipole can be calculated by taking the ratio of photons detected between two or more polarized detection channels^{23,24}. The combination of multiple excitation polarizations and polarized detection channels has been used to measure 3D orientation and rotational mobility²⁴, but the need for multiple polarization modulators, polarizing beamsplitters, and synchronized cameras complicates the adaptation of these methods for SMLM. Recently, the orientation of SM emitters have been measured using their emission pattern, either directly, with modulation by a phase mask, or with modulation by a polarization filter¹³. However, a continuing challenge exists to design an instrument capable of simultaneously resolving the 3D orientation and rotational mobility (or rotational diffusion or constraint) of SMs without angular degeneracy²⁵ while still being compatible with SMLM for localizing the position of those SMs across a large field of view.

Here, we demonstrate a method, termed the Tri-spot point spread function (PSF), for measuring all degrees of freedom related to 3D molecular orientation and rotational mobility. We model a fluorescent molecule as a dipole-like emitter with orientation $\boldsymbol{\mu} = [\mu_x, \mu_y, \mu_z]^T = [\sin \theta \cos \phi, \sin \theta \sin \phi, \cos \theta]^T$, which can be parametrized as μ_x , μ_y and μ_z in Cartesian coordinates or as polar angle θ and azimuthal angle ϕ in spherical coordinates.

The recorded image can then be represented using the orientational second-moment vector $\mathbf{M} = [\langle \mu_x^2 \rangle, \langle \mu_y^2 \rangle, \langle \mu_z^2 \rangle, \langle \mu_x \mu_y \rangle, \langle \mu_x \mu_z \rangle, \langle \mu_y \mu_z \rangle]^T$ ^{9,26–30}

$$\mathbf{I}_{\text{img}} = I_0 [\mathbf{XX}_{\text{img}}, \mathbf{YY}_{\text{img}}, \mathbf{ZZ}_{\text{img}}, \mathbf{XY}_{\text{img}}, \mathbf{XZ}_{\text{img}}, \mathbf{YZ}_{\text{img}}] [\langle \mu_x^2 \rangle, \langle \mu_y^2 \rangle, \langle \mu_z^2 \rangle, \langle \mu_x \mu_y \rangle, \langle \mu_x \mu_z \rangle, \langle \mu_y \mu_z \rangle]^T \quad (1)$$

where \mathbf{I}_{img} is the image of the dipole emitter on the camera, and \mathbf{XX}_{img} , ..., \mathbf{YZ}_{img} are termed the basis images of the microscope, that is, the image produced by an emitter exhibiting each orientation component. The basis images can be computed for any imaging system using vectorial diffraction models²⁹. A cascade of events produces each recorded photon: 1) an SM absorbs a photon at a certain orientation $\boldsymbol{\mu}_{\text{abs}}$; 2) it diffuses rotationally during the molecule's excited state lifetime; and 3) it emits a photon while at an orientation $\boldsymbol{\mu}$. Summing multiple fluorescence photons results in a second-moment vector \mathbf{M} of the molecule's orientation trajectory integrated over one camera frame. The angle brackets $\langle \cdot \rangle$ denote a temporal average or the equivalent ensemble average taken over the orientation domain. Further, if the molecule's rotational diffusion is symmetric around a certain average orientation $[\bar{\mu}_x, \bar{\mu}_y, \bar{\mu}_z]$ and the rotational relaxation time is much shorter than the fluorescence lifetime, the elements of \mathbf{M} can be represented using 4 parameters, $\bar{\mu}_x$, $\bar{\mu}_y$, $\bar{\mu}_z$ and rotational constraint γ ³¹ (Supplementary info 3.1). If the rotational correlation time is longer than the fluorescence lifetime, then γ may be interpreted as an effective rotational constraint or anisotropy factor that depends on both molecular rotation and the illumination polarization³¹. A

rotational constraint γ of unity represents a completely immobile emitter, while for the case of a freely rotating emitter, $\gamma = 0$ and all the cross terms $\langle \mu_i \mu_j \rangle_{i \neq j}$ in \mathbf{M} are equal to zero.

Our imaging system (Figure S1A) includes a polarization beam splitter (PBS) to separate light into two imaging channels, and the Tri-spot phase mask (Figure 1A) is placed in the back focal plane (BFP) in both channels. Due to the geometry of our imaging system and reflective spatial light modulator, the PSF in the x -polarized channel (Figure S1C) is rotated clockwise by 90° relative to that in the y channel (Figure S1D). The fluorescence in both channels is captured by the same image sensor.

For analyzing images of the Tri-spot PSF, we integrate the total photons contained within the 3 spots in each polarized image, resulting in six photon measurements for each molecule. The resulting six-element image vector $\mathbf{I}(I_0, \bar{\mu}_x, \bar{\mu}_y, \bar{\mu}_z, \gamma) = I_0 \mathbf{B} \mathbf{M}(\bar{\mu}_x, \bar{\mu}_y, \bar{\mu}_z, \gamma)$ is a linear combination of the six-by-six basis-image matrix \mathbf{B} . The Tri-spot PSF was designed so that each column of \mathbf{B} is linearly independent and has similar energy (Figure S3), which guarantees a one-to-one correspondence between \mathbf{I} and \mathbf{M} and maximizes the precision of measuring each second moment. We built a maximum-likelihood (ML) estimator to estimate the average orientation $\bar{\mu}_x, \bar{\mu}_y, \bar{\mu}_z$ and the rotational constraint γ from any image \mathbf{I} (Supplemental info 2.1). When the estimator is unbiased at sufficiently high signal-to-background ratio (Figure S5), its performance using simulated images of emitters with various orientations is close to the theoretical limit given by the Cramér-Rao lower bound (CRLB)³². For 3000 photons captured from a fixed SM with 10 background photons/pixel, the Tri-spot PSF achieves an average orientation $\bar{\mu}_x$ measurement precision of 0.06 (7° polar angle and 8° azimuthal angle in spherical coordinates) and rotational constraint γ measurement precision of 0.20 (to provide some physical intuition, this γ is equivalent to a cone half-width uncertainty of 14° for a molecule uniformly diffusing within a cone).

We measured the orientation of single Atto 647N molecules embedded in a thin layer (87 ± 15 nm [mean \pm std.] thickness) of polymethyl methacrylate (PMMA) on a glass coverslip using the Tri-spot PSF in focus. We then used the measured orientation to correct dipole-induced localization bias when using the standard PSF in SMLM. When rotationally fixed, dipole radiation patterns from SMs lead to a systematic lateral (xy) localization bias that increases with defocus (z)^{10,33,34}. The size and direction of this bias is a function of molecular orientation. Thus, accurately measuring a molecule's orientation enables this mislocalization bias to be calculated and removed using a post-processing algorithm⁸.

We used our ML estimator to measure the orientation of each SM and found that the fitted Tri-spot images (Figures 1B,C(ii), S8D) match closely the camera images (Figures 1B,C(i), S8C). The orientation measurements (Figures S8E,F) were used to predict each molecule's localization bias ($\Delta x, \Delta y$) as a function of z using our vectorial diffraction model. Since each

detection channel in our microscope is linearly polarized, we expect localization biases in the x -polarized channel to be largest along the x direction and biases along the y direction to be largest in the y channel (Figure S9). ThunderSTORM³⁵ was used to localize the standard PSF image of each molecule at each defocus position, thereby quantifying each SM's experimental localization bias. The predicted localization bias matches the experimentally-measured bias (Figures 1D,E, S8G,H) to within the experimental localization precision for 95% of all z positions and molecules. We observed localization biases as large as 30 nm for ± 200 nm defocus (Figures 1D,E). Applying the Tri-spot's localization correction reduces this bias to 7 ± 6 nm (mean \pm std.), which is within the localization precision of 13 nm for 2500 photons detected at $z = \pm 200$ nm, thereby restoring the localization accuracy of the imaging system.

Since emission anisotropy causes the localization biases quantified above, it is important to characterize the anisotropy of any emitter used for measuring and calibrating optical aberrations^{36–39}. It is widely assumed that fluorescent beads behave as ideal point sources, especially those that are smaller than the diffraction limit ($\sim \lambda/2NA \approx 250$ nm), but very little is known about their emission anisotropy or heterogeneity. The Tri-spot PSF is ideally suited for quantifying this anisotropy, because the second-moment vector \mathbf{M} measured from each individual bead directly represents the orientation distribution of the ensemble of molecules contained within it. Measuring \mathbf{M} as a function of excitation polarization provides additional insight into depolarization behaviors among the fluorophores within each bead.

Using the Tri-spot PSF, we imaged 20-nm and 100-nm diameter beads embedded in a thin layer (34 ± 14 nm) of polyvinyl alcohol (PVA) sequentially pumped by x - and y -polarized light (Figures 2A,B). Using our ML estimator, we measured a larger effective rotational constraint for 20 nm beads (median $\gamma = 0.52$) than that for 100 nm beads (median $\gamma = 0.38$, Figure 2C). This measurement is consistent with the expectation that the fewer number of fluorophores within the smaller bead results in a fluorescence emission anisotropy more similar to that of a fixed SM and hence a larger effective rotational constraint. Interestingly, both 100-nm and 20-nm beads do not exhibit emission patterns characteristic of isotropic emitters (i.e., γ close to zero). In fact, the measured effective rotational constraint of 20-nm beads suggests that they could exhibit a localization bias of ~ 50 nm when defocused by 200 nm (Figure S9C).

The measured anisotropy factor γ , or effective rotational constraint, of fluorescent beads is a convolution of the distribution of molecular orientations within the bead with the probability of pumping those molecules with polarized light. However, within many material or biological systems, such as fluorescent beads, nanoscale emitters are not accurately modeled by a symmetrically rotating dipole with a certain rotational constraint. We therefore utilize direct basis matrix inversion to measure the full emission anisotropy, i.e., all six second moments, of the fluorescent beads given by $\mathbf{M} = \mathbf{B}^{-1}\mathbf{I}/I_0$.

The Tri-spot PSF image of a typical 100-nm bead does not change significantly under different pumping polarizations; the normalized change in spot brightnesses between x-polarized and y-polarized pumps $\left| \frac{I_{x\text{-pump}}}{|I_{x\text{-pump}}|} - \frac{I_{y\text{-pump}}}{|I_{y\text{-pump}}|} \right| = 5\%$ (Figure 2A).

However, that of a typical 20-nm bead changes much more (14%, Figure 2B). To further quantify this effect, we define δ , the angular rotation of the second-moment vector \mathbf{M} in response to a rotation in pumping polarization given by

$$\delta = \cos^{-1} \frac{\mathbf{M}_{x\text{-pump}} \cdot \mathbf{M}_{y\text{-pump}}}{\|\mathbf{M}_{x\text{-pump}}\| \|\mathbf{M}_{y\text{-pump}}\|} \quad (2)$$

where $\mathbf{M}_{x\text{-pump}}$ and $\mathbf{M}_{y\text{-pump}}$ are the second-moment vectors measured in response to x-polarized and y-polarized excitation light, respectively. We generally expect δ to decrease as γ increases; that is, for a fixed SM emitter ($\gamma = 1$), there is no change in emission pattern when changing pump polarization ($\delta_{\text{fix}} = 0$, Figure S10, Supplementary Discussion). We expect that an isotropic emitter (i.e., an ensemble of independent fixed fluorescent molecules) should emit with varying orientational second moments depending on how they are pumped ($\delta_{\text{iso}} = 50.48^\circ$, Supplementary info 3.2); that is, anisotropic pumping can cause an isotropic emitter to emit anisotropically. Interestingly, our measurements of normalized $\hat{\delta} = \delta/\delta_{\text{iso}}$ (Figure 2D) show that 20-nm beads exhibit a larger second-moment rotation (median $\hat{\delta} = 0.29$) than 100-nm beads (median $\hat{\delta} = 0.08$). This measurement suggests that there is a depolarization mechanism between molecules within the 100-nm beads, such as homo-Förster Resonance Energy Transfer⁴⁰ or rotational relaxation during the fluorescence lifetime³¹, that causes polarized excitation to result in emitted fluorescence that is more isotropic than expected. This depolarization effect is much weaker within 20-nm beads. The Tri-spot PSF is capable of detecting this depolarization because its orientation measurements are independent of excitation polarization, and unlike conventional fluorimeters, the Tri-spot PSF is sensitive enough to detect the emission anisotropy of single fluorescent nanoparticles and SMs.

Single-particle tracking is commonly used in materials science and biophysics to provide insights into the modes of motion of the target object, which may be diffusive, confined, or even motor-directed. Differentiating translational motions from rotational ones has revealed, for example, the fundamental mechanics of the movement of individual molecular motors¹⁸. A strength of the Tri-spot PSF is its capability to measure the rotational and translational diffusion simultaneously of many SMs within a field of view. To demonstrate, we used the Tri-spot PSF to image single Atto 647N molecules embedded in a thin polyvinylpyrrolidone (PVP) film (54 ± 15 nm) in 10-min intervals as they were exposed to humid air.

When the PVP film is exposed to humid air, the spots of the Tri-spot PSF change dramatically in relative brightness (Figures 3(i),(ii)), thereby demonstrating changes in molecular orientation (Supplementary info 3.1). The decreasing effective rotational constraint of embedded fluorescent probes over time, for example from 10 to 60 minutes for molecule 1, is evidence of the polymer network softening and swelling as the moisture slowly penetrates the film. Interestingly, the heterogeneity across

SMs in their measured rotational constraints (Figures 3(iii), S13C-G) suggests that the swelling is non-uniform across the film, even at long timescales. SMs have exhibited increasing translational diffusion when exposed to increasing humidity⁴¹.

However, we observe no correlation between rotational anisotropy and lateral diffusion, measured as the average displacement jump Δr between frames using Tri-spot images (Figures 3(iii), S13C-G, Supplementary info 4.1). The effective rotational constraint γ of molecules 1 and 2 decreased by 0.05 and 0.01 over 50 minutes (an increase of 15° and 7° in cone half-width if the molecule is uniformly diffusing within a cone, Figures 3(iii)), while no significant increase in translational diffusion over the same time period was observed.

Our time-lapse imaging also tracked the average orientation of each molecule (Figures 3(iv), S13C-G), quantifying rotational diffusion over both slow timescales (\sim minutes between each interval) and faster timescales (\sim seconds across camera frames, depicted as ellipses drawn at the initial and end time points in Figures 3(iv), S13C-G). This slow-scale rotation is distinct from our measurements of anisotropy factor γ , which quantify rotational diffusion within a single camera frame (50 ms). The rotational constraint of molecule 1 ($\gamma = 0.95 \pm 0.07$ [mean \pm std.], 15° cone half-angle, Figure 3A(iii), $t = 60$ min) is similar to that of molecule 2 ($\gamma = 0.99 \pm 0.02$, 7° cone half-angle, Figure 3B(iii), $t = 50$ min), but molecule 1 rotates much less than molecule 2 does over 50 minutes (23° for molecule 1, Figure 3A(iv), vs. 63° for molecule 2, Figure 3B(iv)). Observations of other molecules also show that smaller effective rotational constraints γ within a single frame does not necessarily lead to more rotation over long timescales (Figures S13C-G). Interestingly, molecule 7 rotates by 80° within 1 hour although its rotational constraint is not significantly larger than that of molecules 3-6, which all rotate less than 50° . Therefore, a unique strength of the Tri-spot PSF is its capability of quantifying both average orientation between camera frames and rotational movement within each camera frame, rather than requiring multiple acquisitions as in absorption-based measurements. It also allows measurements of rotational diffusion of many molecules simultaneously across a large field of view, compared to higher-speed methods that measure these orientational parameters one molecule at a time⁴². This ability is enabled by our direct engineering of the Tri-spot PSF to encode all 6 components of the second-moment vector \mathbf{M} into its images with maximum sensitivity.

In summary, we report the design of a Tri-spot PSF that accurately and precisely measures the 3D orientation and rotational mobility of fluorescent emitters within one camera frame. The Tri-spot PSF achieves an average orientation precision of 5° and an average precision of 0.20 in rotational constraint (a cone-width precision of 14°) for 3000 photons detected from a single molecule. We demonstrated experimentally that the Tri-spot's orientation measurements are sufficiently accurate to reduce anisotropy-induced localization bias from 30 nm to 7 nm for an SM 200 nm out of focus. The Tri-spot's sensitivity to all orientational degrees of freedom shows that both 100-nm and 20-nm diameter fluorescent beads do not emit light isotropically

and reveals that the larger beads exhibit stronger depolarization effects. The Tri-spot PSF is also compatible with SMLM and SM-tracking techniques and measured the rotational and translational diffusion of dye molecules embedded within a softening polymer film. The ability to fully quantify the 3D orientation, rotational constraint, and translational diffusion of SMs could significantly benefit nanoscale studies across biology and materials science, including interrogating protein-protein interactions, elucidating mechanisms of cargo transport along and across cell membranes, and understanding interactions between fluorophores and nanoparticles⁴³. Further refinements will make it possible to measure the z position of point-like emitters, such that SMLM with the Tri-spot PSF will provide super-resolved images of 3D location, 3D orientation, and rotational constraint of any molecules or nanoparticles of interest.

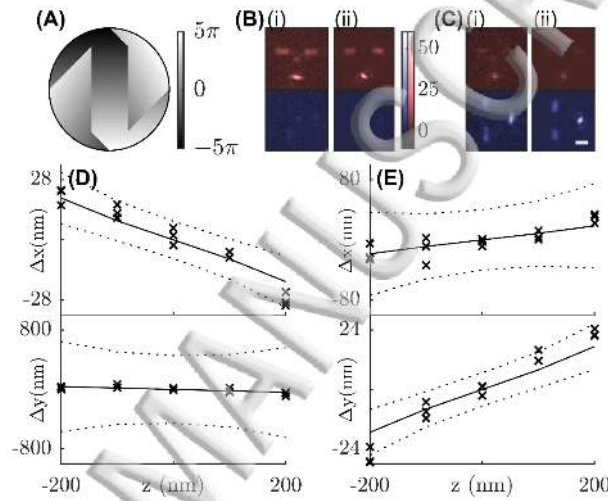


Figure 1. (A) Tri-spot Phase mask. Colorbar: phase (rad). Orientation measurements of Atto 647N (B) molecule 1 and (C) molecule 2. Representative (i) captured and (ii) fitted Tri-spot PSF image of each SM. Red: x -polarized channel; Blue: y -polarized channel. Scale bar: $1\ \mu\text{m}$; Color bar: photons detected. Measured localization bias (cross) along the x -axis in the x -polarized channel and the y -axis in the y -polarized channel at different z positions for (D) molecule 1 and (E) molecule 2 using the standard PSF. The solid line represents the predicted lateral translation from the Tri-spot's orientation measurements, and the dashed line marks the experimental localization precision (± 1 std. dev.).

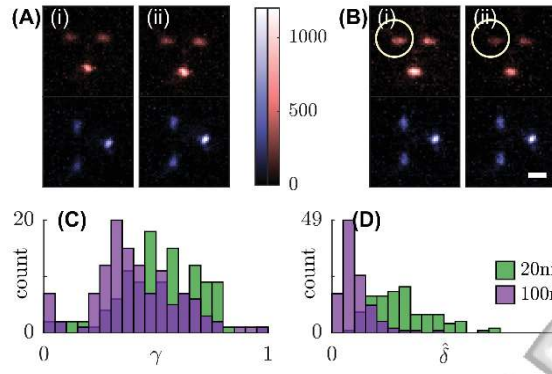


Figure 2. Anisotropy and rotation of the orientational second moment vector of fluorescent beads in response to linearly-polarized excitation. Sum of 100 Tri-spot PSF images of a single (A) 100-nm and (B) 20-nm bead using (i) x- and (ii) y-polarized excitation. Circle highlights the change in spot brightness. (C) Rotational constraint γ and (D) normalized rotation $\hat{\delta}$ in response to x- and y-polarized excitation of 118 fluorescent beads. Green, 20-nm beads; purple, 100-nm beads. Scale bar: 1 μm ; Color bar: photons detected.

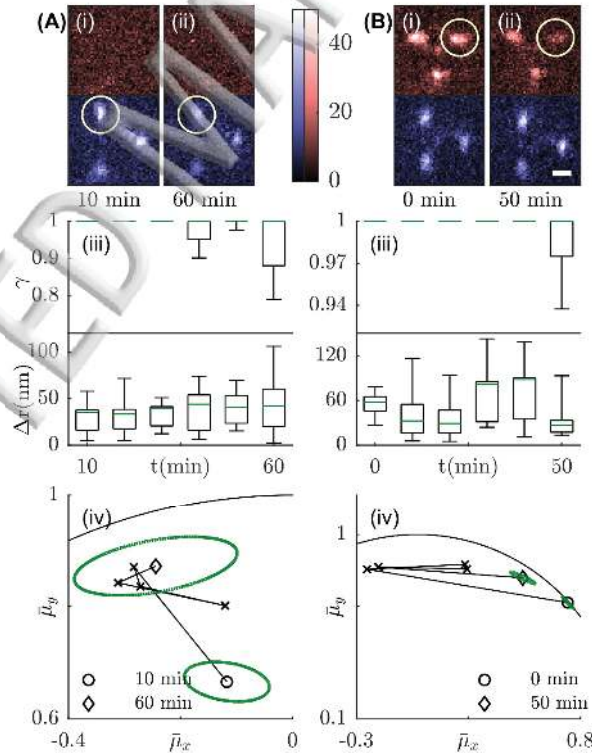


Figure 3. Effective rotational constraint, lateral diffusion, and orientation tracking of Atto 647N molecules embedded in a thin PVP film under continuous exposure to humid air. Tri-spot images of (A) molecule 1 and (B) molecule 2 at the (i) beginning

and (ii) end of time-lapse imaging. Circle highlights the change in spot brightness. The change of (iii) measured anisotropy factor (γ) and lateral movement (Δr) over 50 min. The estimated rotational constraint has a cutoff value of 1 (Supplementary info 4.4). Green: median; Box: first and third quartile; Error bar: minimum and maximum. (iv) The orientation trajectory over 50 min. Circle represents the beginning, and diamond represents the end of the time-lapse measurement. Dashed green ellipse represents the covariance matrix in estimated orientation $(\bar{\mu}_x, \bar{\mu}_y)$ measured at the beginning and the end points. Molecule 1 rotates from $(-0.12 \pm 0.06, 0.67 \pm 0.03)$ (mean \pm std.) to $(-0.24 \pm 0.12, 0.87 \pm 0.04)$, and molecule 2 rotates from $(0.73 \pm 0.03, 0.66 \pm 0.03)$ to $(0.51 \pm 0.05, 0.78 \pm 0.03)$ over 50 min. Solid curve marks the orientation domain $\bar{\mu}_x^2 + \bar{\mu}_y^2 \leq 1$. Scale bar: 1 μm ; Color bar: photons detected.

SUPPLEMENTARY MATERIAL

See the supplementary material for materials and methods, design of the Tri-spot PSF, a theoretical image formation model, detection and estimation of the Tri-spot PSF, and additional discussion and figures.

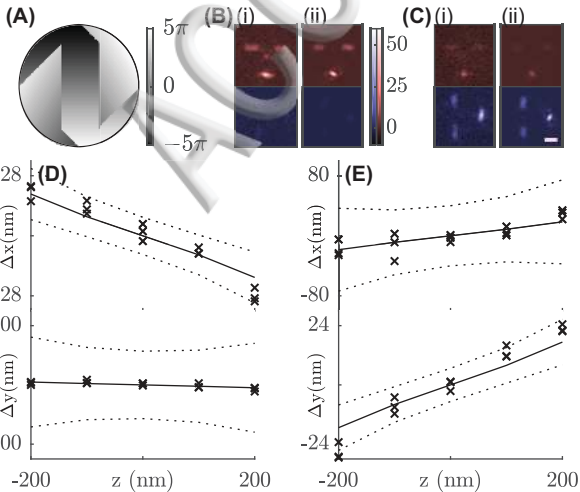
ACKNOWLEDGMENTS

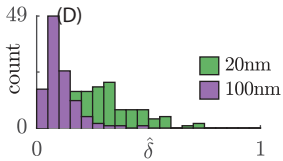
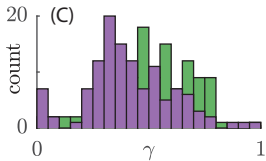
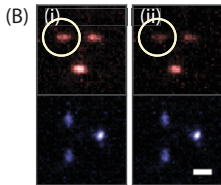
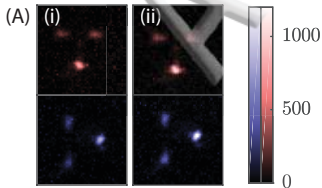
Research reported in this publication was supported by the National Science Foundation under grant number ECCS-1653777 and by the National Institute of General Medical Sciences of the National Institutes of Health under grant number R35GM124858.

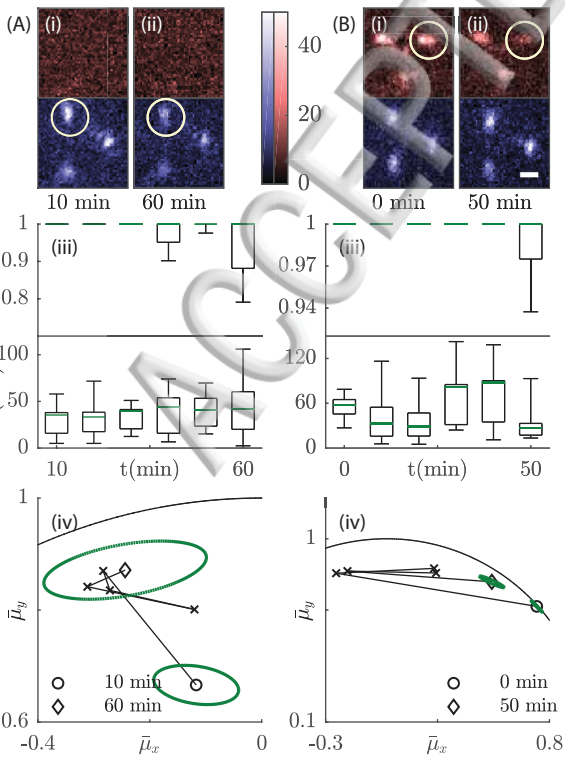
REFERENCES

- ¹ A. Yildiz, J.N. Forkey, S.A. McKinney, T. Ha, Y.E. Goldman, and P.R. Selvin, *Science* **300**, 2061 (2003).
- ² A. Pertsinidis, Y. Zhang, and S. Chu, *Nature* **466**, 647 (2010).
- ³ J.C. Vaughan, S. Jia, and X. Zhuang, *Nat. Methods* **9**, 1181 (2012).
- ⁴ F. Huang, T.M.P. Hartwich, F.E. Rivera-Molina, Y. Lin, W.C. Duim, J.J. Long, P.D. Uchil, J.R. Myers, M. a Baird, W. Mothes, M.W. Davidson, D. Toomre, and J. Bewersdorf, *Nat. Methods* **10**, 653 (2013).
- ⁵ E. Betzig, G.H. Patterson, R. Sougrat, O.W. Lindwasser, S. Olenych, J.S. Bonifacino, M.W. Davidson, J. Lippincott-Schwartz, and H.F. Hess, *Science* **313**, 1642 (2006).
- ⁶ M.J. Rust, M. Bates, and X. Zhuang, *Nat. Methods* **3**, 793 (2006).
- ⁷ S.T. Hess, T.P.K. Girirajan, and M.D. Mason, *Biophys. J.* **91**, 4258 (2006).
- ⁸ M.P. Backlund, M.D. Lew, A.S. Backer, S.J. Sahl, G. Grover, A. Agrawal, R. Piestun, and W.E. Moerner, *Proc. Natl. Acad. Sci.* **109**, 19087 (2012).
- ⁹ A.S. Backer, M.Y. Lee, and W.E. Moerner, *Optica* **3**, 659 (2016).
- ¹⁰ J. Engelhardt, J. Keller, P. Hoyer, M. Reuss, T. Staudt, and S.W. Hell, *Nano Lett.* **11**, 209 (2011).
- ¹¹ M.D. Lew, M.P. Backlund, and W.E. Moerner, *Nano Lett.* **13**, 3967 (2013).
- ¹² M.D. Lew and W.E. Moerner, *Nano Lett.* **14**, 6407 (2014).
- ¹³ M.P. Backlund, M.D. Lew, A.S. Backer, S.J. Sahl, and W.E. Moerner, *ChemPhysChem* **15**, 587 (2014).
- ¹⁴ T. Ha, T. Enderle, D.S. Chemla, P.R. Selvin, and S. Weiss, *Phys. Rev. Lett.* **77**, 3979 (1996).
- ¹⁵ T. Ha, J. Glass, T.H. Enderle, D.S. Chemla, and S. Weiss, *Phys. Rev. Lett.* **80**, 2093 (1998).

- ¹⁶ H. Sosa, E.J.G. Peterman, W.E. Moerner, and L.S.B. Goldstein, Nat. Struct. Biol. **8**, 540 (2001).
- ¹⁷ E.J.G. Peterman, H. Sosa, L.S.B. Goldstein, and W.E. Moerner, Biophys. J. **81**, 2851 (2001).
- ¹⁸ J.N. Forkey, M.E. Quinlan, M. Alexander Shaw, J.E.T. Corrie, and Y.E. Goldman, Nature **422**, 399 (2003).
- ¹⁹ D. Hu, J. Yu, K. Wong, B. Bagchi, P.J. Rossky, and P.F. Barbara, Nature **405**, 1030 (2000).
- ²⁰ K.D. Weston and L.S. Goldner, J. Phys. Chem. B **105**, 3453 (2001).
- ²¹ N.B. Bowden, K.A. Willets, W.E. Moerner, and R.M. Waymouth, Macromolecules **35**, 8122 (2002).
- ²² N. Karedla, S.C. Stein, D. Hähnel, I. Gregor, A. Chizhik, and J. Enderlein, Phys. Rev. Lett. **115**, 173002 (2015).
- ²³ J.T. Fourkas, Opt. Lett. **26**, 211 (2001).
- ²⁴ J.N. Forkey, M.E. Quinlan, and Y.E. Goldman, Biophys. J. **89**, 1261 (2005).
- ²⁵ J.R. Lakowicz, *Principles of Fluorescence Spectroscopy* (Springer US, Boston, MA, 2006).
- ²⁶ M. Böhmer and J. Enderlein, J. Opt. Soc. Am. B **20**, 554 (2003).
- ²⁷ M.A. Lieb, J.M. Zavislan, and L. Novotny, J. Opt. Soc. Am. B **21**, 1210 (2004).
- ²⁸ D. Axelrod, J. Microsc. **247**, 147 (2012).
- ²⁹ A.S. Backer and W.E. Moerner, J. Phys. Chem. B **118**, 8313 (2014).
- ³⁰ A.S. Backer and W.E. Moerner, Opt. Express **23**, 4255 (2015).
- ³¹ S. Stallinga, J. Opt. Soc. Am. A **32**, 213 (2015).
- ³² T.K. Moon and W.C. Stirling, *Mathematical Methods and Algorithms For Signal Processing* (2000).
- ³³ J. Enderlein, E. Toprak, and P.R. Selvin, Opt. Express **14**, 8111 (2006).
- ³⁴ S. Stallinga and B. Rieger, Opt. Express **18**, 24461 (2010).
- ³⁵ M. Ovesny, P. Křík, J. Borkovec, Z. Vindrych, and G.M. Hagen, Bioinformatics **30**, 2389 (2014).
- ³⁶ O. Azucena, J. Crest, S. Kotadia, W. Sullivan, X. Tao, M. Reinig, D. Gavel, S. Olivier, and J. Kubby, Opt. Lett. **36**, 825 (2011).
- ³⁷ D.E. Milkie, E. Betzig, and N. Ji, Opt. Lett. **36**, 4206 (2011).
- ³⁸ R. McGorty, J. Schnitzbauer, W. Zhang, and B. Huang, Opt. Lett. **39**, 275 (2014).
- ³⁹ A. von Diezmann, M.Y. Lee, M.D. Lew, and W.E. Moerner, Optica **2**, 985 (2015).
- ⁴⁰ C.C. Gradinaru, D.O. Marushchak, M. Samim, and U.J. Krull, Analyst **135**, 452 (2010).
- ⁴¹ S. Bhattacharya, D.K. Sharma, S. Saurabh, S. De, A. Sain, A. Nandi, and A. Chowdhury, J. Phys. Chem. B **117**, 7771 (2013).
- ⁴² J.F. Beausang, D.Y. Shroder, P.C. Nelson, and Y.E. Goldman, Biophys. J. **104**, 1263 (2013).
- ⁴³ K.A. Willets, A.J. Wilson, V. Sundaresan, and P.B. Joshi, Chem. Rev. **117**, 7538 (2017).







Supplementary Material for “Imaging the three-dimensional orientation and rotational mobility of fluorescent emitters using the Tri-spot point spread function”

Oumeng Zhang, Jin Lu, Tianben Ding, and Matthew D. Lew

Electrical and Systems Engineering, Washington University in St. Louis, St. Louis, Missouri, 63130, USA

1. Materials and methods

1.1 Materials

Polyvinyl alcohol (PVA, MW 146,000-186,000, Sigma-Aldrich, Cat: 363103), Polymethyl methacrylate (PMMA, MW 996,000, Sigma-Aldrich, Cat: 182265), Polyvinylpyrrolidone (PVP, MW 10,000, Sigma-Aldrich, Cat: PVP10), toluene (ThermoFisher, Cat: 16790), dimethyl sulfoxide (DMSO, ThermoFisher, Cat: 20688), Atto 647N amine (Sigma-Aldrich, Cat: 95349), 100 nm fluorescent beads (ThermoFisher, F8803), and 20 nm fluorescent beads (ThermoFisher, F8760) were used as received. Glass coverslips (Marienfeld-Superior, Cat: 0107052) were used as the imaging substrate. Ultrapure water ($>18\text{ M}\Omega\cdot\text{cm}$) was obtained through a Millipore water purification system (MilliporeSigma, Cat: MPPG040001) and used for all aqueous solutions.

1.2 Sample Preparation

All the glass coverslips used for imaging were ozone cleaned (Novascan, PSD series) for 15 min to remove fluorescent residues. Atto 647N was first dissolved in DMSO as stock solution, and further diluted in toluene or H_2O . The final concentration of Atto 647N was adjusted to ensure the fluorescent molecules were uniformly and sparsely distributed in the field of view during imaging.

1.2.1 Localization bias correction and fluorescent bead imaging

Thin polymer films containing fluorescent probes or beads were prepared by spin-coating (MTI Corporation, VTC-100, 2500 rpm, 40 s) 20 μL of polymer solution onto the ozone-cleaned coverslips. Three different solutions were used, including (1) Atto 647N in 10 mg/mL PMMA in toluene solution, (2) 100 nm fluorescent beads (1:3000 v/v dilution) in 10 mg/mL PVA in H_2O solution, and (3) 20 nm fluorescent beads (1:107 v/v dilution) in 10 mg/mL PVA in H_2O solution. The prepared coverslip was mounted inside a chamber (Bioscience Tools, CSC) on the microscope stage with one drop ($\sim 20\text{ }\mu\text{L}$) of immersion oil on top of the polymer film to ensure refractive index match.

1.2.2 Single-molecule (SM) rotational constraint and orientation tracking

Three-layer polymer films were prepared by sequentially spin coating (2500 rpm, 40 s): (i) 20 μL of 10 mg/mL PVP in H_2O solution, (ii) 20 μL of Atto 647N in 10 mg/mL PVP in H_2O solution, and (iii) another 20 μL 10 mg/mL PVP in H_2O solution on an ozone-cleaned coverslip. The coverslip was heated to 90 $^\circ\text{C}$ for 30 minutes to remove residual solvent and then mounted inside a chamber (ALA Scientific, MS-CPC) on the microscope stage.

1.2.3 Measure the thickness of polymer films.

The thickness of the polymer films spin-coated on the coverslip was measured using a profilometer (KLA-Tencor Alpha-Step D-100). The scan was performed at a speed of 0.07 mm/s. Multiple measurements were performed on each polymer film with 0.10 mg stylus force.

1.3 Fluorescence microscopy

A home-built microscope system with a 60x, 1.3 NA objective lens (Olympus, UPLSAPO 60XS2) and achromatic tube lens ($f=200$ mm) was used to perform SM imaging (Figure S1(a)). The 3D position of the sample was controlled by a piezoelectric nanopositioning stage (Physik Instrumente P-545.3C7). A polarization beam splitter (PBS, Meadowlark Optics, BB-100-VIS) was used to separate fluorescence images into x - and y -polarized channels. The back focal plane of both channels was projected onto a spatial light modulator (SLM, Meadowlark Optics, 256 XY Phase Series) that generates the Tri-spot phase mask by the first lens ($f=150$ mm) of a 4f system. The image plane of both polarization channels was then projected onto different regions of an sCMOS camera (Hamamatsu ORCA-flash4.0 C11440-22CU).

1.3.1 Localization bias correction

Sample (1) prepared in Section 1.2.1 was excited using a 637-nm laser (Coherent OBIS 637, 1.13 kW/cm^2 peak intensity and circularly polarized at the sample). The imaging sequence consisted of (i) one frame (150 ms for molecule 1-2 in Figure 1, or 75 ms for molecule 3-6 in Figure S8) of the Tri-spot PSF in focus; (ii) one frame of the standard PSF at five defocus (z) positions ($z = \{-200, -100, 0, 100, 200\}$ nm) ; (iii) repeat steps (i) and (ii) three times, and (iv) additional 100 frames using the Tri-spot PSF to ensure a single-step photobleaching event was observed.

1.3.2 Fluorescent bead imaging

Samples (2) and (3) prepared in Section 1.2.1 were excited using a 514-nm laser (Coherent Sapphire 514, 273.8 W/cm^2 peak intensity at the sample). The linearity of the laser polarization at the sample was tuned using a polarization compensator (Thorlabs, SBC-VIS), resulting in a polarization ratio of $\sim 150:1$ for both x - and y -polarized modes. To acquire a similar signal level to 20-nm beads, the peak pump power for 100-nm beads was reduced to 13.7 W/cm^2 by applying a 1.3 OD filter. For

each field of view, 100 frames (10 ms/frame) under x -polarized excitation and 100 frames under y -polarized excitation were captured. For each bead, all 100 frames using x - and y -polarized pumping light were used to estimate $\mathbf{M}_{x\text{-pump}}$ and $\mathbf{M}_{y\text{-pump}}$ (eq. 2), and all 200 frames were used to estimate γ in Figure 2. The 100 measurements were separated into a first and second set of 50 frames under x -polarized pumping light to estimate $\mathbf{M}_{x,1}$ and $\mathbf{M}_{x,2}$ (eq. S22). The first 50 frames using y -polarized pumping light were used to estimate \mathbf{M}_y (eq. S22).

1.3.3 Second-moment vector rotation δ of fixed SM emitters

We followed the procedure in Section 1.2.1 to prepare Atto 647N in PMMA and excited these molecules with a 637-nm laser (0.57 kW/cm² peak intensity at the sample). We captured (i) two frames of Tri-spot images under x -polarized excitation, (ii) followed by one frame of under y -polarized excitation, and (iii) finally 100 more Tri-spot images with circular pumping to ensure a single-step photobleaching event was observed.

1.3.4 SM rotational constraint and orientation tracking

The sample prepared in Section 1.2.2 was mounted in a closed perfusion chamber (ALA Scientific, MS-CPC) and purged with humid air from a homemade gas washing system. The humidity of the airflow into the chamber was monitored by a humidity meter (Fisher Scientific, Cat: 1464984). The imaging sequence consisted of (i) 10 frames (50 ms/frame) using the Tri-spot PSF (637 nm, 1.13 kW/cm² peak intensity and circularly polarized at the sample) at the ambient humidity level (~20%, RH), (ii) 10 frames every 10 minutes with humid air (~70%, RH) continuously purging for 1 hour, and (iii) additional 490 frames as necessary to verify single-step photobleaching. The excitation laser was only turned on when the images were captured. Before each 10-frame acquisition, we refocused the microscope, aiming for the spots of the Tri-spot PSF to resemble an equilateral triangle as closely as possible. Comparison of our experimental data to simulated images indicates that all measurements were taken within ~100 nm of perfect focus.

2. Design of the Tri-spot PSF

The distribution of fluorescence photons in both the back focal plane and image plane can be represented as a linear combination of basis images and an orientational second-moment vector \mathbf{M}^{1-5} , given by

$$\mathbf{I}_{\text{BFP}} = I_0 [\mathbf{XX}_{\text{BFP}}, \mathbf{YY}_{\text{BFP}}, \mathbf{ZZ}_{\text{BFP}}, \mathbf{XY}_{\text{BFP}}, \mathbf{XZ}_{\text{BFP}}, \mathbf{YZ}_{\text{BFP}}] \underbrace{\left[\langle \mu_x^2 \rangle, \langle \mu_y^2 \rangle, \langle \mu_z^2 \rangle, \langle \mu_x \mu_y \rangle, \langle \mu_x \mu_z \rangle, \langle \mu_y \mu_z \rangle \right]}_{\mathbf{M}}^T \quad (\text{S1})$$

$$\mathbf{I}_{\text{img}} = I_0 [\mathbf{XX}_{\text{img}}, \mathbf{YY}_{\text{img}}, \mathbf{ZZ}_{\text{img}}, \mathbf{XY}_{\text{img}}, \mathbf{XZ}_{\text{img}}, \mathbf{YZ}_{\text{img}}] \underbrace{\left[\langle \mu_x^2 \rangle, \langle \mu_y^2 \rangle, \langle \mu_z^2 \rangle, \langle \mu_x \mu_y \rangle, \langle \mu_x \mu_z \rangle, \langle \mu_y \mu_z \rangle \right]}_{\mathbf{M}}^T \quad (\text{S2})$$

where $\mathbf{XX}_{\text{BFP}}, \dots, \mathbf{YZ}_{\text{BFP}}$ and $\mathbf{XX}_{\text{img}}, \dots, \mathbf{YZ}_{\text{img}}$ are termed the basis images of the back focal plane (BFP) and image plane, respectively. Such images can be calculated as the outer product of the electric fields produced by combinations of x -, y -, and z -orientated dipoles⁶. We note this image-formation model holds for any rotational correlation time τ_r and fluorescence lifetime τ_f ; the effect of rotational diffusion can be included when calculating the time-averaged second moments⁵, as discussed in SI Section 3.1. These time-averaged moments may depend on higher-order moments, especially if the illumination laser is polarized and partially coherent and rotational diffusion is slow⁶.

Our strategy for orientation estimation will be to encode the magnitude of each component of \mathbf{M} within a focused spot of a multi-spot PSF. Therefore, we integrate the photons within each spot of the PSF within the image plane (see SI Section 4.2 for details), and we represent the recorded image as $\mathbf{I} = [I_1, I_2, \dots, I_N]^T$ and the basis images as $\mathbf{XX} = [XX_1, XX_2, \dots, XX_N]^T$, etc., where I_i and XX_i are the total photons contained within the i th spot of the recorded image and basis images, respectively, and N is the total number of spots on both polarization channels. After integration, Eq. S2 becomes:

$$\mathbf{I} = I_0 \underbrace{\begin{bmatrix} XX_1 & YY_1 & ZZ_1 & XY_1 & XZ_1 & YZ_1 \\ XX_2 & YY_2 & ZZ_2 & XY_2 & XZ_2 & YZ_2 \\ \vdots & \vdots & \vdots & \vdots & \vdots & \vdots \\ XX_N & YY_N & ZZ_N & XY_N & XZ_N & YZ_N \end{bmatrix}}_{\mathbf{B}} \mathbf{M} \quad (\text{S3})$$

where \mathbf{B} is a N -by-six basis-image matrix.

Since $\langle \mu_x^2 \rangle + \langle \mu_y^2 \rangle + \langle \mu_z^2 \rangle = 1$ due to the definition of μ , there are a total of five degrees of freedom to describe molecular orientation and rotational mobility of a dipole emitter. To estimate all 5 orientational degrees of freedom (plus the brightness of a molecule) using the relative intensities of a multi-spot PSF, we need the PSF to contain at least six total spots across both polarization channels of the imaging system. Inspired by the bisected⁷ phase mask, we initially set the phase mask of the Tri-spot PSF to partition the back focal plane into three regions as shown in Figure S2(a). The basis-image matrix of this design is

$$\mathbf{B}_{\text{init}} = \begin{bmatrix} 0.34 & 0.00 & 0.06 & 0.00 & 0.00 & 0.03 \\ 0.34 & 0.00 & 0.06 & 0.00 & 0.00 & -0.03 \\ 0.32 & 0.00 & 0.11 & 0.00 & 0.01 & 0.00 \\ 0.00 & 0.34 & 0.06 & 0.00 & 0.03 & 0.00 \\ 0.00 & 0.34 & 0.06 & 0.00 & -0.03 & 0.00 \\ 0.00 & 0.32 & 0.11 & 0.00 & 0.00 & 0.00 \end{bmatrix} \quad (\text{S4})$$

where $\text{rank}(\mathbf{B}_{\text{init}}) = 5$. Due to the symmetry of back focal plane intensity distribution, this design has no sensitivity to $\langle \mu_x \mu_y \rangle$ (Figure S2(b)). A full-rank basis image matrix \mathbf{B} ($\text{rank}(\mathbf{B}) = 6$) is required so that the PSF is sensitive to all orientational degrees of freedom. Since the energy of the \mathbf{XY}_{BFP} basis is concentrated at the corners of the BFP (Figure S2(c)), we combine the partition shapes in Figures S2(a) and S2(c) to improve the $\langle \mu_x \mu_y \rangle$ sensitivity of the Tri-spot mask. The basis matrix of the new partition (Figure S2(d)) is

$$\mathbf{B}_{\text{design}} = \begin{bmatrix} 0.26 & 0.00 & 0.04 & 0.03 & 0.10 & 0.02 \\ 0.26 & 0.00 & 0.04 & 0.03 & -0.10 & -0.02 \\ 0.46 & 0.00 & 0.15 & -0.05 & 0.00 & 0.00 \\ 0.00 & 0.26 & 0.04 & -0.03 & 0.02 & -0.10 \\ 0.00 & 0.26 & 0.04 & -0.03 & -0.02 & 0.10 \\ 0.00 & 0.46 & 0.15 & 0.05 & 0.00 & 0.00 \end{bmatrix} \quad (\text{S5})$$

where $\text{rank}(\mathbf{B}_{\text{design}}) = 6$. This basis-image matrix shows that this design of the Tri-spot PSF is capable of measuring all orientational second moments, while the bisected⁷ and quadrated⁸ PSF, whose basis matrices given by eq. S6, cannot.

$$\begin{aligned} \text{rank}(\mathbf{B}_{\text{bisected}}) &= \text{rank} \left(\begin{bmatrix} 0.49 & 0.01 & 0.12 & 0.00 & 0.00 & 0.04 \\ 0.49 & 0.01 & 0.12 & 0.00 & 0.00 & -0.04 \\ 0.01 & 0.49 & 0.12 & 0.00 & 0.04 & 0.00 \\ 0.01 & 0.49 & 0.12 & 0.00 & -0.04 & 0.00 \end{bmatrix} \right) = 4 \\ \text{rank}(\mathbf{B}_{\text{quadrated}}) &= \text{rank} \left(\begin{bmatrix} 0.25 & 0.00 & 0.08 & -0.05 & 0.21 & -0.03 \\ 0.25 & 0.00 & 0.08 & 0.05 & -0.21 & -0.03 \\ 0.25 & 0.00 & 0.08 & 0.05 & 0.21 & 0.03 \\ 0.00 & 0.25 & 0.08 & -0.05 & -0.03 & 0.21 \\ 0.00 & 0.25 & 0.08 & 0.05 & -0.03 & -0.21 \\ 0.00 & 0.25 & 0.08 & -0.05 & 0.03 & -0.21 \end{bmatrix} \right) = 5 \end{aligned} \quad (\text{S6})$$

Further, the eigenvalues of the Tri-spot PSF's basis-image matrix $\mathbf{B}_{\text{design}}$ satisfy $\ln(\max|\lambda| / \min|\lambda|) = 1.69$, showing that the PSF has similar sensitivity to all orientational degrees of freedom. Further, the sum of each column of the $|\mathbf{B}_{\text{design}}|$ ranges from 0.22 to 1, exemplifying that each spot of the Tri-spot PSF has a similar brightness (Figure S3(a)).

In our homebuilt microscope, we use one SLM to apply the phase mask to both polarization channels (Figure S1(a)). Consequently, the x -axis in the pupil plane of the y -polarized channel is flipped compared to the design (Figure S3(i)), and the y -channel XY and XZ basis images (Figures S3(v)-S3(vi)) are inverted in amplitude compared to the designed PSF. The experimental basis-image matrix is therefore given by

$$\mathbf{B}_{\text{exp}} = \begin{bmatrix} 0.26 & 0.00 & 0.04 & 0.03 & 0.10 & 0.02 \\ 0.26 & 0.00 & 0.04 & 0.03 & -0.10 & -0.02 \\ 0.46 & 0.00 & 0.15 & -0.05 & 0.00 & 0.00 \\ 0.00 & 0.26 & 0.04 & 0.03 & -0.02 & -0.10 \\ 0.00 & 0.26 & 0.04 & 0.03 & 0.02 & 0.10 \\ 0.00 & 0.46 & 0.15 & -0.05 & 0.00 & 0.00 \end{bmatrix} \quad (\text{S7})$$

where $\text{rank}(\mathbf{B}_{\text{exp}}) = 5$.

When using an MLE to estimate average orientation and rotational constraint (Section 4.2), the measurement comprises four degrees of freedom ($\bar{\mu}_x$, $\bar{\mu}_y$, γ and I_0). Therefore, although this basis-image matrix is not full-rank as we designed, we can still solve this overdetermined problem precisely, accurately, and robustly.

For the second-moment vector rotation (δ) analysis where we directly measure all six dimensions of \mathbf{M} , we use the pseudo-inverse $\mathbf{B}_{\text{exp}}^+$ to find the minimum norm solution to the underdetermined problem:

$$\hat{\mathbf{M}} = \frac{\mathbf{B}_{\text{exp}}^+ \mathbf{s}}{I_0} \quad (\text{S8})$$

where \mathbf{s} represents the counted photons within each spot of the Tri-spot PSF. Molecular orientations, and changes thereof, are encoded in \mathbf{s} , and the inverse of the basis-image matrix acts as a linear operator that maps \mathbf{s} to orientational second moment space. Therefore, although the accuracy and precision of $\hat{\mathbf{M}}$ estimates could be degraded when using \mathbf{B}_{exp} compared to those using $\mathbf{B}_{\text{design}}$, the observed changes δ are sufficiently significant to reveal changes in the emission anisotropy of fluorescent beads under different excitation polarizations. Further, Monte Carlo simulations indicate that measurements of δ are suitably accurate and precise at SBRs typical of fluorescent beads (Fig. S10(e)).

3. Theoretical image formation model

3.1 Symmetric rotation model and maximum likelihood estimator

Consider a mobile dipole $\boldsymbol{\mu} = [\mu_x, \mu_y, \mu_z]^T = [\sin \theta \cos \phi, \sin \theta \sin \phi, \cos \theta]^T$ that rotates around a certain average orientation $\bar{\boldsymbol{\mu}} = [\bar{\mu}_x, \bar{\mu}_y, \bar{\mu}_z]^T = [\sin \bar{\theta} \cos \bar{\phi}, \sin \bar{\theta} \sin \bar{\phi}, \cos \bar{\theta}]^T$ over time. We assume that the rotation is much faster than the acquisition time t of one camera frame, which implies ergodicity, that is, there exists an orientation distribution probability density function $P_{\theta, \phi}(\theta, \phi)$ so that the temporal average of $\boldsymbol{\mu}$ is equal to the spatial orientation average over this distribution. We assume that the distribution is symmetric around the average orientation $\bar{\boldsymbol{\mu}}$. The second moment of the molecular orientation can therefore be calculated as:

$$\langle \mu_i \mu_j \rangle = \int_0^{2\pi} \int_0^{\frac{\pi}{2}} \mu_i(\theta, \phi) \mu_j(\theta, \phi) P_{\theta, \phi}(\theta, \phi) \sin \theta d\theta d\phi \quad (\text{S9})$$

where $i, j = x, y, z$ in eq. S9.

To ease the calculation of this integral, we rotate the average orientation $\bar{\boldsymbol{\mu}}$. First, we rotate about the z axis by an angle of $-\bar{\phi}$, then rotate about y axis by an angle of $-\bar{\theta}$. After the rotation, the average orientation lies along the z axis. The relation between the dipole orientation before the rotation $\boldsymbol{\mu}$ and after the rotation $\boldsymbol{\mu}'$ is:

$$\begin{aligned} \boldsymbol{\mu} &= \mathbf{R} \boldsymbol{\mu}' = \begin{bmatrix} \cos \bar{\phi} & -\sin \bar{\phi} & 0 \\ \sin \bar{\phi} & \cos \bar{\phi} & 0 \\ 0 & 0 & 1 \end{bmatrix} \begin{bmatrix} \cos \bar{\theta} & 0 & \sin \bar{\theta} \\ 0 & 1 & 0 \\ -\sin \bar{\theta} & 0 & \cos \bar{\theta} \end{bmatrix} \boldsymbol{\mu}' \\ &= \begin{bmatrix} \cos \bar{\theta} \cos \bar{\phi} & -\sin \bar{\phi} & \sin \bar{\theta} \cos \bar{\phi} \\ \cos \bar{\theta} \sin \bar{\phi} & \cos \bar{\phi} & \sin \bar{\theta} \sin \bar{\phi} \\ -\sin \bar{\theta} & 0 & \cos \bar{\theta} \end{bmatrix} \boldsymbol{\mu}' \end{aligned} \quad (\text{S10})$$

Therefore, we can write a matrix that includes all second moments as:

$$\mathbf{M}_{\text{reshape}} = \langle \boldsymbol{\mu} \boldsymbol{\mu}^T \rangle = \begin{bmatrix} \langle \mu_x^2 \rangle & \langle \mu_x \mu_y \rangle & \langle \mu_x \mu_z \rangle \\ \langle \mu_x \mu_y \rangle & \langle \mu_y^2 \rangle & \langle \mu_y \mu_z \rangle \\ \langle \mu_x \mu_z \rangle & \langle \mu_y \mu_z \rangle & \langle \mu_z^2 \rangle \end{bmatrix} = \mathbf{R} \langle \boldsymbol{\mu}' \boldsymbol{\mu}'^T \rangle \mathbf{R}^T \quad (\text{S11})$$

Since the rotated average orientation $\bar{\boldsymbol{\mu}}'$ is along the z axis and the distribution of $\boldsymbol{\mu}'$ is symmetric around $\bar{\boldsymbol{\mu}}'$, the result of the integration of eq. S11 in the rotated frame can be written as:

$$\begin{aligned} \langle \mu'_x \mu'_y \rangle &= \langle \mu'_x \mu'_z \rangle = \langle \mu'_y \mu'_z \rangle = 0 \\ \langle \mu'^2_x \rangle &= \langle \mu'^2_y \rangle = \lambda \end{aligned} \quad (\text{S12})$$

Thus, we can calculate the second moments of the molecular orientation for this symmetric distribution model as:

$$\mathbf{M}_{\text{reshape}} = \mathbf{R} \begin{bmatrix} \lambda & 0 & 0 \\ 0 & \lambda & 0 \\ 0 & 0 & 1 - 2\lambda \end{bmatrix} \mathbf{R}^T \quad (\text{S13})$$

By calculating the matrix multiplication, we have:

$$\begin{aligned}
\langle \mu_x^2 \rangle &= \gamma \bar{\mu}_x^2 + (1 - \gamma)/3 & \langle \mu_x \mu_y \rangle &= \gamma \bar{\mu}_x \bar{\mu}_y \\
\langle \mu_y^2 \rangle &= \gamma \bar{\mu}_y^2 + (1 - \gamma)/3 & \langle \mu_x \mu_z \rangle &= \gamma \bar{\mu}_x \bar{\mu}_z \\
\langle \mu_z^2 \rangle &= \gamma \bar{\mu}_z^2 + (1 - \gamma)/3 & \langle \mu_y \mu_z \rangle &= \gamma \bar{\mu}_y \bar{\mu}_z
\end{aligned} \tag{S14}$$

where $\gamma = 1 - 3\lambda$ in eq. S14 denotes the rotational constraint of the molecule.

We note that the rotational correlation time of Atto 647N molecules in water is approximately 0.8 ns⁹, while their fluorescence lifetime is on the order of 3-4 ns¹⁰⁻¹². For Atto 647N doped in a PVP film where polymer crosslinks constrain the movement of each fluorophore, we may surmise that the rotational correlation time becomes longer than the fluorescence lifetime. In this case, the symmetric rotation model becomes approximate, and the emission second-moment \mathbf{M} becomes a function of both molecular rotation and illumination polarization. We therefore interpret γ as an effective rotational constraint or anisotropy factor.

3.2 Second moments for an isotropic emitter under linear pumping polarization

In this section, we present a simple analysis to quantify how anisotropic excitation affects the emission anisotropy of an emitter that can be modeled as the sum of many independent transition dipole moments uniformly distributed across all orientations. The excitation probability of such an emitter has a \cos^2 dependence on the angle between the dipole orientation and pump polarization, that is, when the emitter is excited by x-polarized light, the absorption probability $P(\theta, \phi) \propto \mu_x^2$. The second moment can then be calculated as:

$$\begin{aligned}
\langle \mu_i \mu_j \rangle &= \int_0^{2\pi} \int_0^{\pi/2} \mu_i(\theta, \phi) \mu_j(\theta, \phi) P(\theta, \phi) \sin \theta \, d\theta d\phi \\
&= \frac{\int_0^{2\pi} \int_0^{\pi/2} \mu_i(\theta, \phi) \mu_j(\theta, \phi) \mu_x^2(\theta, \phi) \sin \theta \, d\theta d\phi}{\int_0^{2\pi} \int_0^{\pi/2} \mu_x^2(\theta, \phi) \sin \theta \, d\theta d\phi}
\end{aligned} \tag{S15}$$

The calculated second moments are:

$$\begin{aligned}
\langle \mu_x^2 \rangle &= 0.6 & \langle \mu_y^2 \rangle &= \langle \mu_z^2 \rangle = 0.2 \\
\langle \mu_x \mu_y \rangle &= \langle \mu_x \mu_z \rangle = \langle \mu_y \mu_z \rangle &= 0
\end{aligned} \tag{S16}$$

Thus, an isotropic emitter excited by linearly polarized light exhibits an orientational second moment distribution that is non-uniform. Its emission is equivalent to the sum of three dipoles: one dipole oriented along the x axis with amplitude 0.6, one oriented along the y axis with amplitude 0.2, and one along the z axis with amplitude 0.2. If any of the transition dipoles interact with one another within this emitter under x-polarized excitation, then we may expect the second moments, and therefore the emission anisotropy, to be more uniform than that in eq. S16. We note that according to eq. S14, γ is equal to zero

in eq. S16 due to the chosen excitation polarization direction. However, if the excitation beam is not parallel with the x or y axes, then $\gamma \neq 0$. Therefore, γ is affected by both molecular orientation and excitation polarization and should be interpreted as an effective rotational constraint or anisotropy factor.

4. Detection and estimation

4.1 Tri-spot PSF detection

A detection process is required for localizing the Tri-spot PSF and accurately counting photons within each spot. The first step is to register three spots within each polarization channel. ThunderSTORM is used to localize all spots within a field of view (Figure S4(a)). We then calculate the distance and angle between every two spots and keep the spot pairs that appropriately map to distances and angles between spots of the Tri-spot PSF. The center of the PSF is determined by each pair of spots (Figure S4(b)). If three spots are detected within one Tri-spot PSF, we calculate the average among all three recovered center locations weighted by the spot intensity as the center of the Tri-spot PSF. For simulated fixed dipole emitters, the calculated center location of the Tri-spot PSF varied by less than 35.5 nm for all orientations (20.7 nm on average) for ± 100 nm defocus.

Dual-channel registration is performed by generating a registration map from images of randomly-distributed 100-nm fluorescent beads on the surface of a coverslip. We image 271 beads across a $50\text{ }\mu\text{m}$ by $50\text{ }\mu\text{m}$ field of view, and calculate the bead positions by averaging the localizations across 8-10 frames from ThunderSTORM. All possible lines joining pairs of bead positions across the two channels are drawn. Control points for two channel registration are selected by comparing the obtained lines, and keeping the largest ensemble of them with similar lengths and slopes. These control points are then used to generate global 2D mapping functions (second-degree polynomials) for x - and y -coordinate transformation using the MATLAB function `fitgeotrans`. This map, which provides pixel-level registration accuracy, is used for automatic grouping of Tri-spot PSFs between channels and is not used for precise nm-scale localization. When tracking the lateral movements of the standard PSF (localization bias correction experiment, e.g. Figure 1) or Tri-spot PSF (Δr measurement in the SM rotational constraint and orientation-tracking experiment, e.g. Figure 3), positions were tracked independently within each polarization channel.

4.2 Symmetric rotation model and maximum likelihood estimator

As discussed in Section 3.1, both the molecular orientation and rotational constraint are described by four parameters: $\bar{\mu}_x$, $\bar{\mu}_y$, $\bar{\mu}_z$ and γ under the constraint $\bar{\mu}_x^2 + \bar{\mu}_y^2 + \bar{\mu}_z^2 = 1$, we can write a maximum-likelihood (ML) estimator based on this model.

Due to the size of the Tri-spot PSF, the background fluorescence often varies across the PSF region. Therefore, we estimate the background of the entire field of view by isolating rows and columns of the image, least-squares fitting them to the sum of two Gaussian functions (MATLAB function `gauss2`), and averaging the fitted Gaussians together (Figure S4(c)).

We count the total number of signal photons and total number of background photons within each spot region (Figure S4(d)) as $\mathbf{s} = [s_1, \dots, s_6]$ and $\mathbf{b} = [b_1, \dots, b_6]$. The total number of fitted Gaussian background photons within each spot region are considered as both the recorded and expected background photons. The spot regions are chosen so that 0th order leakage,

which usually contains less than 5% of total fluorescence in the PSF due to the imperfect phase modulation by the SLM, is excluded.

Since the second-moment matrix of molecular orientation \mathbf{M} can be parameterized by $\bar{\mu}_x$, $\bar{\mu}_y$, $\bar{\mu}_z$ and γ , the image intensity distribution can be written as $I(I_0, \bar{\mu}_x, \bar{\mu}_y, \bar{\mu}_z, \gamma) = I_0 \mathbf{B} \mathbf{M}(\bar{\mu}_x, \bar{\mu}_y, \bar{\mu}_z, \gamma)$. Since photon detection is a Poisson process, we can write the likelihood function as:

$$l(I_0, \bar{\mu}_x, \bar{\mu}_y, \bar{\mu}_z, \gamma) = \prod_{i=1}^6 \frac{(I_i + b_i)^{(s_i + b_i)} e^{-(I_i + b_i)}}{(s_i + b_i)!} \quad (\text{S17})$$

The log likelihood function is therefore given by

$$\Lambda(I_0, \bar{\mu}_x, \bar{\mu}_y, \bar{\mu}_z, \gamma) \propto \sum_{i=1}^6 (s_i + b_i) \ln(I_i + b_i) - (I_i + b_i) \quad (\text{S18})$$

After using the MATLAB function `fmincon` to minimize $-\Lambda(I_0, \bar{\mu}_x, \bar{\mu}_y, \bar{\mu}_z, \gamma)$ under the constraints $\bar{\mu}_x^2 + \bar{\mu}_y^2 + \bar{\mu}_z^2 = 1$ and $\gamma > 0$ given the photon measurements measured by our detector, we obtain the orientation estimates $\bar{\mu}_x$, $\bar{\mu}_y$, $\bar{\mu}_z$ and γ .

4.3 Precision and accuracy for average orientation $\bar{\mu}_x$, $\bar{\mu}_y$ and $\bar{\mu}_z$

The Fisher information matrix of the estimator is given by

$$\mathbf{FI} = \sum_i \frac{1}{I_i + b_i} \begin{bmatrix} \left(\frac{\partial I_i}{\partial \bar{\mu}_x}\right)^2 & \left(\frac{\partial I_i}{\partial \bar{\mu}_x}\right)\left(\frac{\partial I_i}{\partial \bar{\mu}_y}\right) & \left(\frac{\partial I_i}{\partial \bar{\mu}_x}\right)\left(\frac{\partial I_i}{\partial \bar{\mu}_z}\right) & \left(\frac{\partial I_i}{\partial \bar{\mu}_x}\right)\left(\frac{\partial I_i}{\partial \gamma}\right) & \left(\frac{\partial I_i}{\partial \bar{\mu}_x}\right)\left(\frac{\partial I_i}{\partial I_0}\right) \\ \left(\frac{\partial I_i}{\partial \bar{\mu}_x}\right)\left(\frac{\partial I_i}{\partial \bar{\mu}_y}\right) & \left(\frac{\partial I_i}{\partial \bar{\mu}_y}\right)^2 & \left(\frac{\partial I_i}{\partial \bar{\mu}_y}\right)\left(\frac{\partial I_i}{\partial \bar{\mu}_z}\right) & \left(\frac{\partial I_i}{\partial \bar{\mu}_y}\right)\left(\frac{\partial I_i}{\partial \gamma}\right) & \left(\frac{\partial I_i}{\partial \bar{\mu}_y}\right)\left(\frac{\partial I_i}{\partial I_0}\right) \\ \left(\frac{\partial I_i}{\partial \bar{\mu}_x}\right)\left(\frac{\partial I_i}{\partial \bar{\mu}_z}\right) & \left(\frac{\partial I_i}{\partial \bar{\mu}_y}\right)\left(\frac{\partial I_i}{\partial \bar{\mu}_z}\right) & \left(\frac{\partial I_i}{\partial \bar{\mu}_z}\right)^2 & \left(\frac{\partial I_i}{\partial \bar{\mu}_z}\right)\left(\frac{\partial I_i}{\partial \gamma}\right) & \left(\frac{\partial I_i}{\partial \bar{\mu}_z}\right)\left(\frac{\partial I_i}{\partial I_0}\right) \\ \left(\frac{\partial I_i}{\partial \bar{\mu}_x}\right)\left(\frac{\partial I_i}{\partial \gamma}\right) & \left(\frac{\partial I_i}{\partial \bar{\mu}_y}\right)\left(\frac{\partial I_i}{\partial \gamma}\right) & \left(\frac{\partial I_i}{\partial \bar{\mu}_z}\right)\left(\frac{\partial I_i}{\partial \gamma}\right) & \left(\frac{\partial I_i}{\partial \gamma}\right)^2 & \left(\frac{\partial I_i}{\partial \gamma}\right)\left(\frac{\partial I_i}{\partial I_0}\right) \\ \left(\frac{\partial I_i}{\partial \bar{\mu}_x}\right)\left(\frac{\partial I_i}{\partial I_0}\right) & \left(\frac{\partial I_i}{\partial \bar{\mu}_y}\right)\left(\frac{\partial I_i}{\partial I_0}\right) & \left(\frac{\partial I_i}{\partial \bar{\mu}_z}\right)\left(\frac{\partial I_i}{\partial I_0}\right) & \left(\frac{\partial I_i}{\partial \gamma}\right)\left(\frac{\partial I_i}{\partial I_0}\right) & \left(\frac{\partial I_i}{\partial I_0}\right)^2 \end{bmatrix} \quad (\text{S19})$$

and the Cramér-Rao lower bound (CRLB), or the limit of orientation measurement precision of an unbiased estimator is given by

$$\mathbf{CRLB} = \begin{bmatrix} \text{var}(\bar{\mu}_x) & \text{cov}(\bar{\mu}_x, \bar{\mu}_y) & \text{cov}(\bar{\mu}_x, \bar{\mu}_z) & \text{cov}(\bar{\mu}_x, \gamma) & \text{cov}(\bar{\mu}_x, I_0) \\ \text{cov}(\bar{\mu}_x, \bar{\mu}_y) & \text{var}(\bar{\mu}_y) & \text{cov}(\bar{\mu}_y, \bar{\mu}_z) & \text{cov}(\bar{\mu}_y, \gamma) & \text{cov}(\bar{\mu}_y, I_0) \\ \text{cov}(\bar{\mu}_x, \bar{\mu}_z) & \text{cov}(\bar{\mu}_y, \bar{\mu}_z) & \text{var}(\bar{\mu}_z) & \text{cov}(\bar{\mu}_z, \gamma) & \text{cov}(\bar{\mu}_z, I_0) \\ \text{cov}(\bar{\mu}_x, \gamma) & \text{cov}(\bar{\mu}_y, \gamma) & \text{cov}(\bar{\mu}_z, \gamma) & \text{var}(\gamma) & \text{cov}(\gamma, I_0) \\ \text{cov}(\bar{\mu}_x, I_0) & \text{cov}(\bar{\mu}_y, I_0) & \text{cov}(\bar{\mu}_z, I_0) & \text{cov}(\gamma, I_0) & \text{var}(I_0) \end{bmatrix} = \mathbf{FI}^{-1} \quad (\text{S20})$$

The precision of our ML estimator under 3000 signal photons is close to the CRLB for unbiased estimations (Figures S5(c), S6(a),(b)). The biases close to $\bar{\mu}_{x,y,z} = 1$ are the result of estimation constraint $\bar{\mu}_x^2 + \bar{\mu}_y^2 + \bar{\mu}_z^2 = 1$. Both the precision and accuracy improve for larger signals (20000 signal photons and 10 photons/pixel background) (Figures S5(d), S6(c),(d)).

4.4 Calibration of estimation algorithm for rotational constraint γ

Validating our maximum-likelihood estimator using simulated images of SMs shows that the measured rotational constraint γ exhibits a small positive bias for small values of γ . For an isotropic emitter, we expect the three second-moment components $\langle \mu_x \mu_y \rangle$, $\langle \mu_x \mu_z \rangle$, and $\langle \mu_y \mu_z \rangle$ to be strictly zero. However, any measurement noise, for example photon shot noise, will almost certainly result in nonzero estimates of any of the aforementioned second moments, thereby causing the measurement of γ to be nonzero and positive. To characterize the relation between the bias $\gamma - \gamma_{\text{true}}$ and the signal-to-background ratio, we simulated images of emitters at various orientations and SBRs (Figure S7(a)). The exponential curve $\gamma - \gamma_{\text{true}} = a \exp(b \gamma_{\text{true}})$ represents a good fit to the data. We define the SBR as $\text{SBR} = \text{signal}/\sqrt{\text{background}}$. The tuning parameters a and b vary linearly with SBR (Figures S7(b),(c)). Therefore, eq. S21 can be used as calibration equation for improved accuracy in estimating γ .

$$\gamma - \gamma_{\text{true}} = \left(\frac{150.69}{\text{SBR}} + 0.03 \right) \exp((-4.3 \text{ SBR} - 1354.0) \times 10^{-3} \times \gamma_{\text{true}}) \quad (\text{S21})$$

Two examples of the γ calibration are shown in Figure S7(d). We calculate γ_{true} based on the output γ from the ML estimator, which could be greater than one. Then we consider all molecules with γ values greater than one as rotationally fixed ($\gamma = 1$).

5. Supplementary discussion

A fixed SM dipole embedded in PMMA (see Section 1.3.3) with an orientation near the x-axis, which is more efficiently pumped by x-polarized light than by y-polarized light, is shown in Figure S10(a). However, the relative intensities of six spots remain similar after varying pumping polarization. We define the rotation in second-moment vector \mathbf{M} under x-polarized excitation only δ_{xx} and between x-polarized and y-polarized excitation δ_{xy} as

$$\begin{aligned}\delta_{xx} &= \cos^{-1} \left(\frac{\mathbf{M}_{x,1} \cdot \mathbf{M}_{x,2}}{\|\mathbf{M}_{x,1}\| \|\mathbf{M}_{x,2}\|} \right) \\ \delta_{xy} &= \cos^{-1} \left(\frac{\mathbf{M}_{x,2} \cdot \mathbf{M}_y}{\|\mathbf{M}_{x,2}\| \|\mathbf{M}_y\|} \right)\end{aligned}\tag{S22}$$

The measured rotation in orientation for Atto 647N (Figure S10(b)) between x- and y-polarized pumping conditions, $\hat{\delta}_{xy} = 0.70 \pm 0.34$ (median \pm std.), is similar to that under x-polarized pumping only, $\hat{\delta}_{xx} = 0.63 \pm 0.43$. Simulations of fixed dipole emitters under the same SBR show a similar rotation, $\hat{\delta}_{xx,\text{sim}} = 0.67 \pm 0.31$. Further, the asymptotic p-values from the two-sample Kolmogorov-Smirnov tests between $\hat{\delta}_{xx}$ and $\hat{\delta}_{xx,\text{sim}}$ are 0.18 (n=18) and $\hat{\delta}_{xx}$ and $\hat{\delta}_{yy}$ are 0.22 (n=18), indicating significant similarity between these distributions. The agreement between experimental measurements of δ under alternating and constant pumping polarizations, along with simulations, suggests that these data are consistent with molecules being fixed in orientation (median $\gamma = 1$, Figure S10(c)). Due to the low photon budget for single molecules, the precision of measuring δ is much worse than that for fluorescent beads (Figure 2, more than a factor of 100 fewer photons). Despite the decreased precision, there is no significant difference in measured SM orientations under identical versus orthogonal pumping polarizations, suggesting that our assumption that SM emission orientations are unaffected by pumping polarization (i.e., $\delta_{\text{fix}} = 0$) is valid.

We note that a similar measurement for 20-nm beads shows that $\hat{\delta}_{xy}$ is significantly larger than $\hat{\delta}_{xx}$ (Figure S10(d), $p = 4.0 \times 10^{-11}$, n=120), while for 100-nm beads, the difference between the distributions of $\hat{\delta}_{xy}$ and $\hat{\delta}_{xx}$ is much smaller ($p = 1.5 \times 10^{-5}$, n=120). Comparing the distribution of $\hat{\delta}_{xx}$ for 20-nm beads to that for simulated isotropic emitters (Figure S10(d), i.e., ensemble of independent fixed fluorescent molecules) shows that they are less similar than the same comparison for 100-nm beads, indicating that 20-nm beads emit light less isotropically. This observation is consistent with the measured anisotropy factor (Figure 2(c)). The distributions of $\hat{\delta}_{xy}$ for both 20-nm and 100-nm beads also differ from the distribution for simulated isotropic emitters (Figure S10(e)), suggesting that there is a depolarization mechanism within the beads. Further, the median

change of all second moments for both 20-nm and 100-nm beads under orthogonal pumping polarizations is larger than the change under identical pumping polarization (p-values of 4.36×10^{-4} for $|\Delta\langle\mu_x^2\rangle|$ and 12.49×10^{-4} for $|\Delta\langle\mu_y^2\rangle|$ for 20-nm beads and p-values of 0.013 for $|\Delta\langle\mu_x^2\rangle|$ and 4.30×10^{-5} for $|\Delta\langle\mu_y^2\rangle|$ for 100-nm beads, $n=120$), and the emission of 20-nm beads have greater dependence on pumping polarization than 100-nm beads (Figure S11(ii)). The second moments of 100-nm beads change very slightly between pumping conditions (average $p = 0.46$, $n=120$), while we measure larger $\langle\mu_x^2\rangle$ when pumped with x -polarized light (Figure S11(a)) and larger $\langle\mu_y^2\rangle$ when pumped with y -polarized light for 20-nm beads (Figure S11(b), average $p = 0.26$, $n=120$). The second moments of the representative 20-nm bead in Figure 2 also have a greater change in $\langle\mu_x^2\rangle$ and $\langle\mu_y^2\rangle$ between pumping polarizations (0.37 ± 0.01 to 0.26 ± 0.04 , and 0.32 ± 0.02 to 0.41 ± 0.04 , mean \pm std., respectively) than 100-nm bead (0.40 ± 0.02 to 0.37 ± 0.02 , and 0.33 ± 0.01 to 0.33 ± 0.01 , respectively, Figure S12). The relatively constant measurements of second moments under constant pumping polarization, compared to changing pumping polarization, suggests that the excitation polarization is stable during the experiment.

These results again suggest that depolarization effects are stronger in 100-nm beads, which is consistent with our findings in Figure 2.

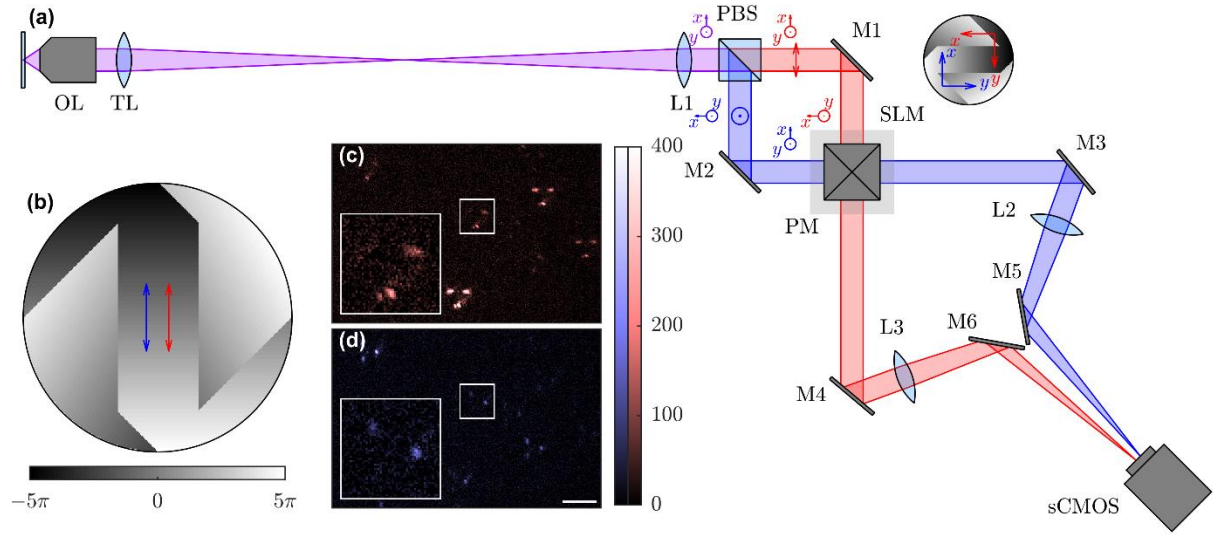


Figure S1. (a) Detailed schematics of the imaging system. Fluorescence was collected by a 60X silicone-immersion objective (OL, 1.3 NA). Afterward, the fluorescence was split by a polarizing beam splitter (PBS) into two orthogonally-polarized channels, and lens L1 ($f = 150$ mm) projects the pupil plane onto a spatial light modulator (SLM) using a square pyramidal mirror (PM). Purple, red, and blue rays depict the emission path before the PBS and the x and y channels after the PBS respectively. Arrows alongside the rays with corresponding colors depict the pupil-plane coordinate system (x, y) in each channel before and after the PBS up to projection onto the SLM. Due to the geometry of the SLM, the (b) Tri-spot phase mask applied to the y -polarized channel is rotated counterclockwise by 90° relative to that in the x -channel. Double-headed arrows depict the electric field polarization direction with respect to mask. After reflection, both (c) x -polarized channel and (d) y -polarized channel were imaged onto different portions of the sCMOS camera by lenses L2 and L3 ($f = 150$ mm). Scale bar: $5\mu\text{m}$; Color bar: photons detected/pixel.

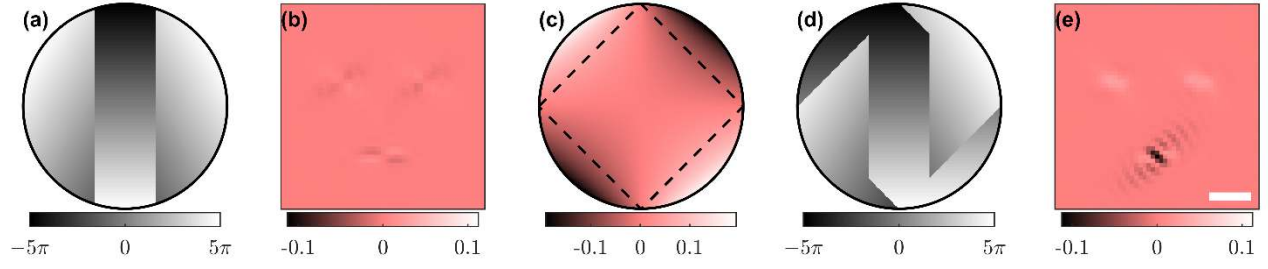


Figure S2. Tri-spot PSF design process. (a) A phase mask that splits light at the back focal plane into three regions and (b) the corresponding XY basis image in the x -polarized channel. (c) The XY basis image of the back focal plane in the x -polarized channel. Dashed lines mark the feature included in the final design of the Tri-spot phase mask. (d) The final Tri-spot phase mask and (e) the corresponding XY basis image in the x -polarized channel. Scale bar: $1\ \mu\text{m}$; Color bar: phase (a,d), intensity normalized to the XX basis image (b,c,e).

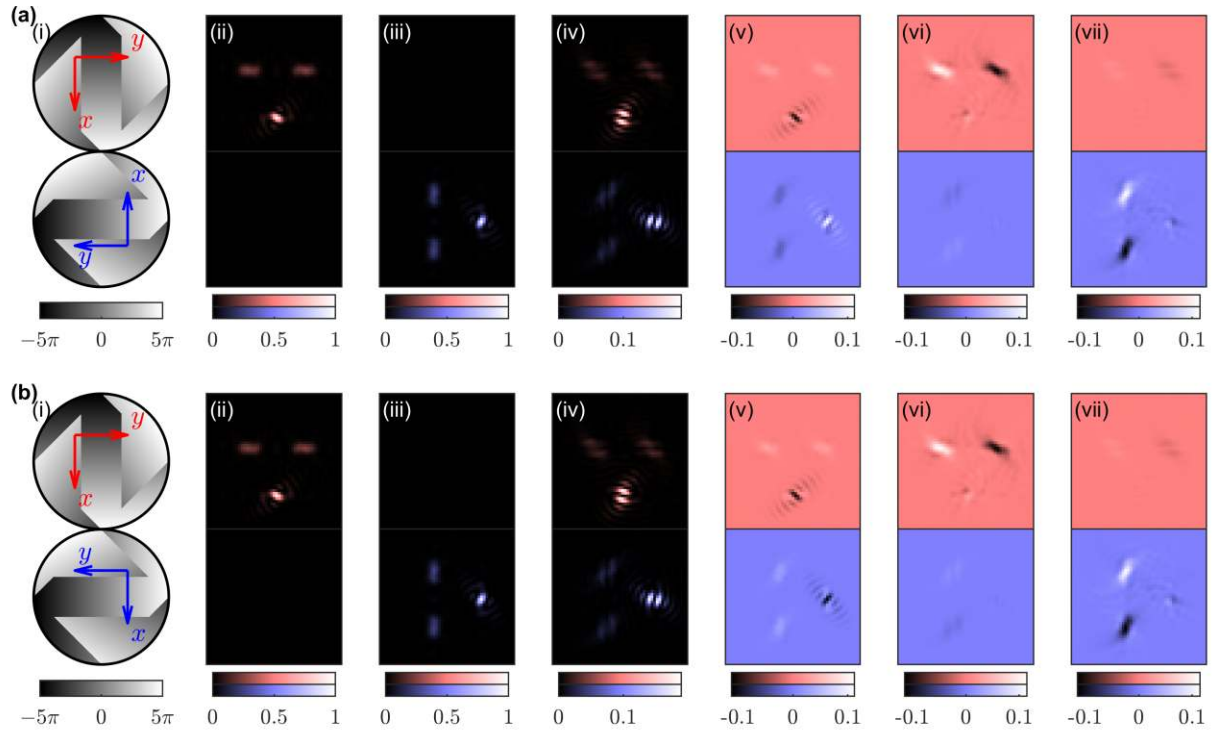


Figure S3. Basis images of (a) the designed Tri-spot PSF (B_{design}) and (b) the Tri-spot PSF in the experimental setup shown in Figure S1 (B_{exp}). (i) The pupil plane coordinate system with respect to the direction of the Tri-spot phase mask. (ii-vii) The XX, YY, ZZ, XY, XZ, and YZ basis images in the (top) x -polarized and (bottom) y -polarized channels. To generate these images, we simulated an ideal imaging system with an objective lens of NA=1.3, an immersion medium of refractive index $n=1.518$, and a dipole emitter of wavelength $\lambda=600$ nm. Scale bar: 1 μm ; Color bar: arbitrary unit.

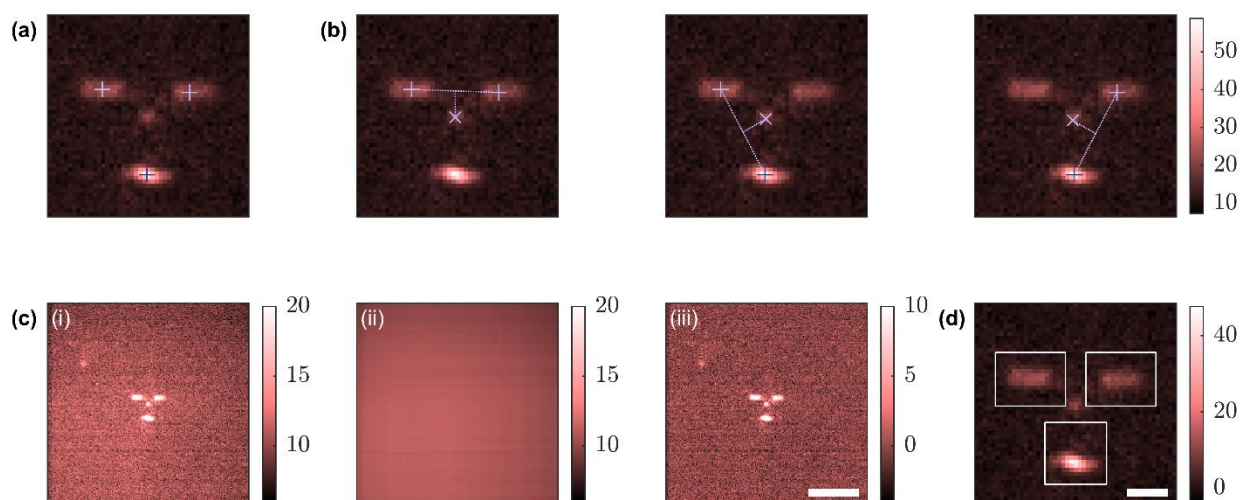


Figure S4. Detection and estimation of the Tri-spot PSF. (a) ThunderSTORM is used to localize all spots. (b) Each spot pair that appropriately maps to distances and angles between spots of the Tri-spot PSF is used to estimate the PSF's center. Cross represents the center location determined by each ThunderSTORM localization pair. These locations are averaged together, weighted by the spot intensity, to generate a final estimate of the molecule's location. (c) (i) The raw image of molecule 1 in Figure 1 in *x*-polarized channel shows a nonuniform background. (ii) The estimated Gaussian background and (iii) the image after background subtraction. Scale bar: 5 μm . (d) We integrate the signal and background photons within each box as the input of our ML estimator. Scale bar: 1 μm .

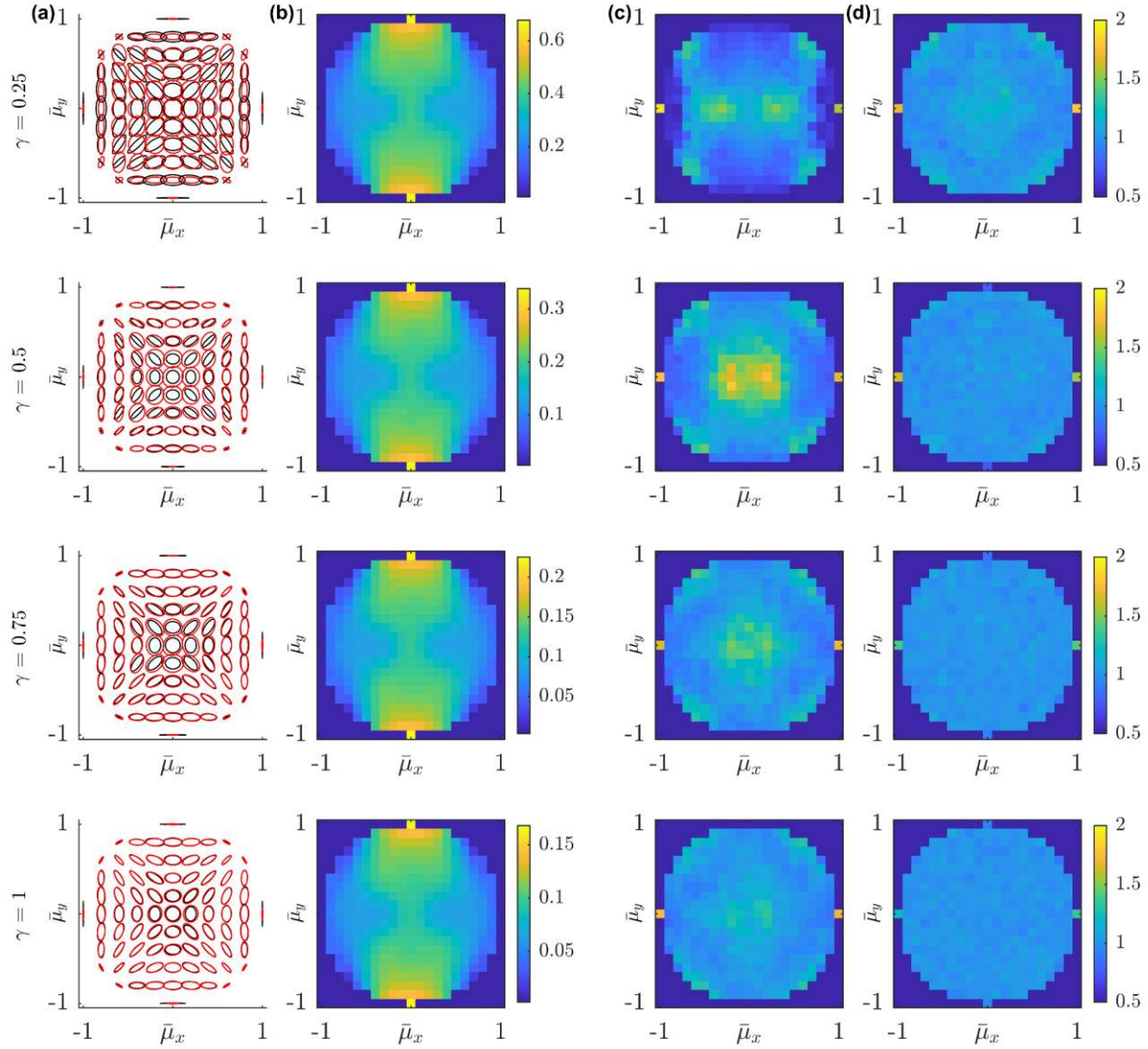


Figure S5. Average orientation measurement precision of the Tri-spot ML estimator using simulated images of molecules with average orientation $\{\bar{\mu}_x, \bar{\mu}_y\} = [-1:0.1:1] \times [-1:0.1:1]$ and rotational constraint $\gamma = [0.25, 0.5, 0.75, 1]$. (a) The measured covariance ellipse and the Cramér-Rao lower bound (CRLB), or the limit of orientation measurement precision. The ellipses are resized to 5%, 10%, 30%, 50% of the original size, respectively. Black: CRLB; Red: measured covariance. (b) The square root of CRLB for $\bar{\mu}_x$ estimation. (c) The ratio between the standard deviation of ML estimates and the square root of the CRLB. 500 images for each $\{\mu_x, \mu_y, \gamma\}$ were generated with 3000 signal photons and 10 photons/pixel background. The ratio between measured standard deviation and square root of CRLB shows that the ML estimator's performance is close to the theoretical limit for unbiased estimations, and (d) the performance improves for 20000 signal photons and 10 photons/pixel background.

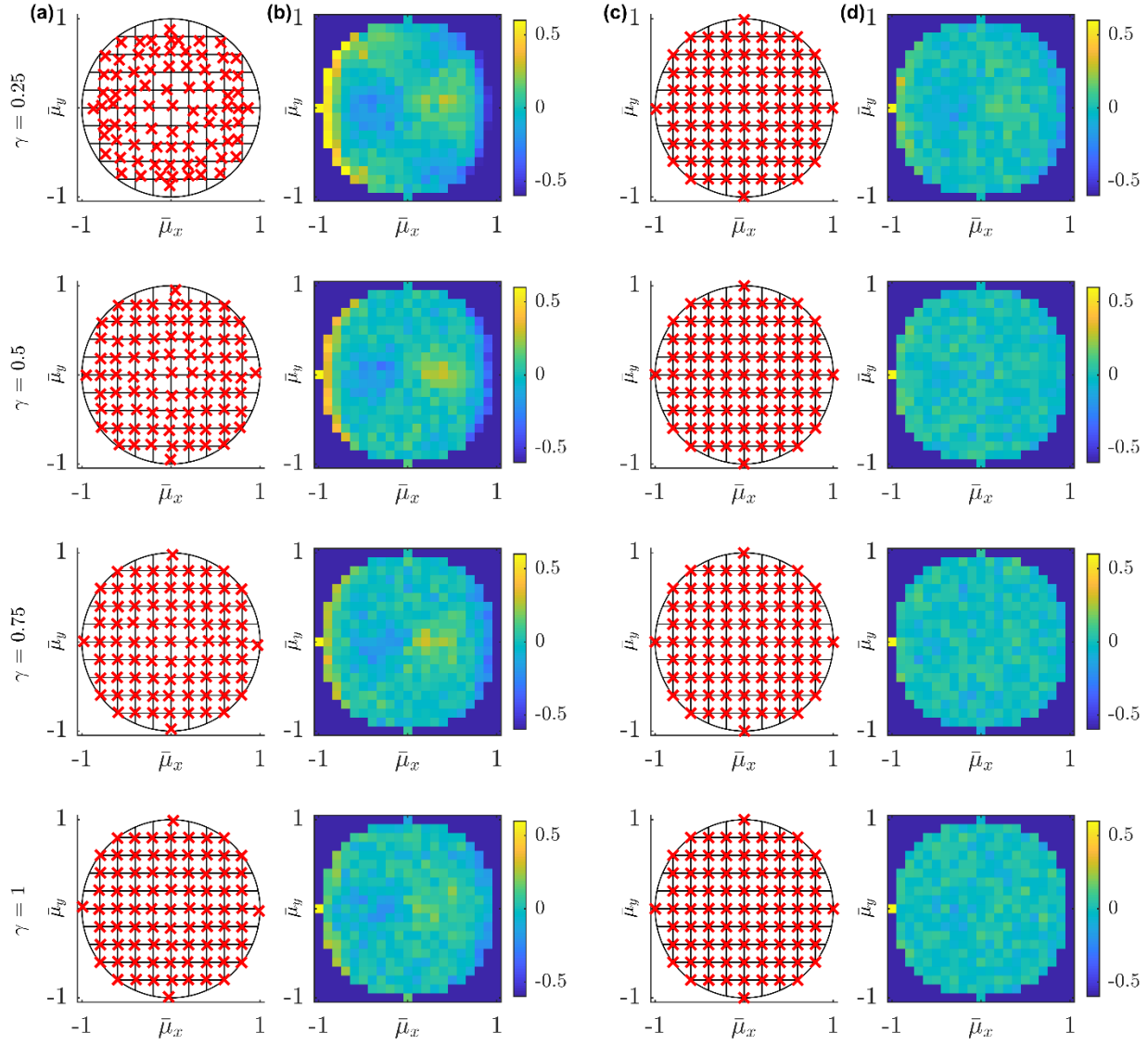


Figure S6. Average orientation $\bar{\mu}_x$ measurement accuracy of the Tri-spot ML estimator using simulated images of molecules with average orientation $\{\bar{\mu}_x, \bar{\mu}_y\} = [-1:0.1:1] \times [-1:0.1:1]$ and rotational constraint $\gamma = [0.25, 0.5, 0.75, 1]$. (a) The measured median and the ground truth for each $\{\bar{\mu}_x, \bar{\mu}_y\}$. Red cross: measured median; Black grid: ground truth. (b) The ratio between the bias of $\bar{\mu}_x$ estimates and the square root of the CRLB. 500 images for each $\{\mu_x, \mu_y, \gamma\}$ were generated with 3000 signal photons and 10 photons/pixel background. Both (c) the bias and (d) its ratio to the square root of the CRLB decrease at 20000 signal photons and 10 photons/pixel background.

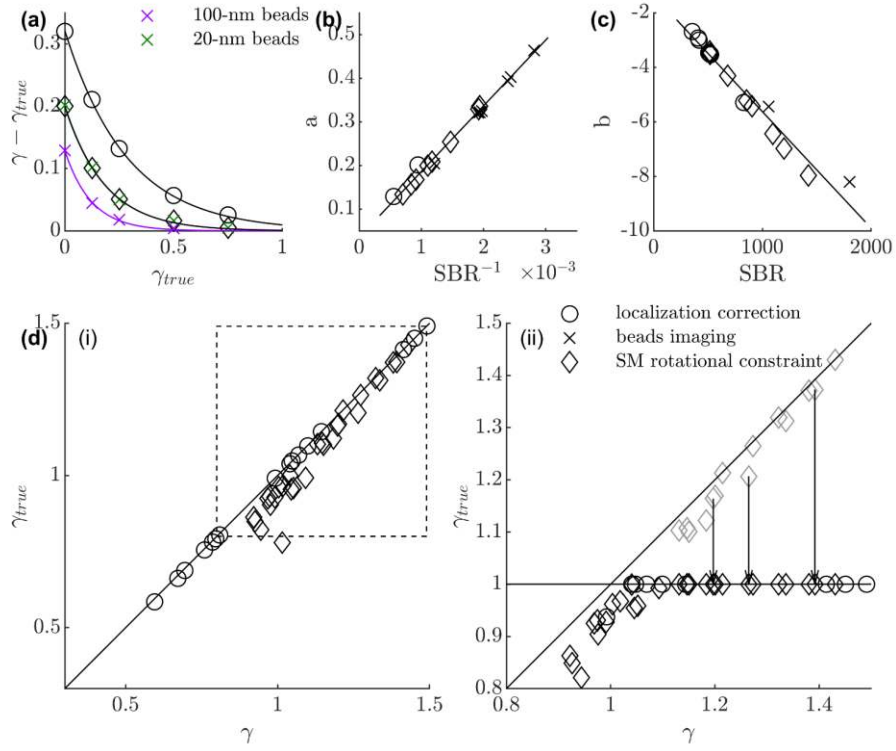


Figure S7. (a) Calibration of the Tri-spot ML estimator for rotational constraint using simulated images of molecules with average orientation $\{\bar{\mu}_x, \bar{\mu}_y\} = [-1: 0.1: 1] \times [-1: 0.1: 1]$ and rotational constraint $\gamma = \{0, 0.125, 0.25, 0.5, 0.75\}$. One hundred images for each $\{\mu_x, \mu_y, \gamma\}$ were generated with the same SBR as in the experiments (see Table S1). Circle: average SBR from the localization bias-correction experiment; diamond: average SBR from the SM rotational constraint and orientation-tracking experiment; cross: average SBR of 100-nm (purple) and 20-nm (green) beads from the fluorescent bead-imaging experiment. Solid line represents the fitted curve $\gamma - \gamma_{\text{true}} = a \exp(b\gamma_{\text{true}})$. Both parameters (b) a and (c) b vary linearly with SBR. Circles and diamonds represent the fitted a and b for the SBR of each individual molecule from the SM experiments, and crosses mark the fitted parameters under the average SBR of 100-nm and 20-nm beads. Solid line represents the linear fit (Eq. S21). (d) Two-step calibration of two representative molecules from Figures 1,3. (i) γ calibration using eq. S21 and (ii) all molecules with γ greater than 1 are considered as fixed dipoles ($\gamma = 1$). Circles: Molecule 1 from Figure 1; Diamond: Molecule 1 from Figure 3.

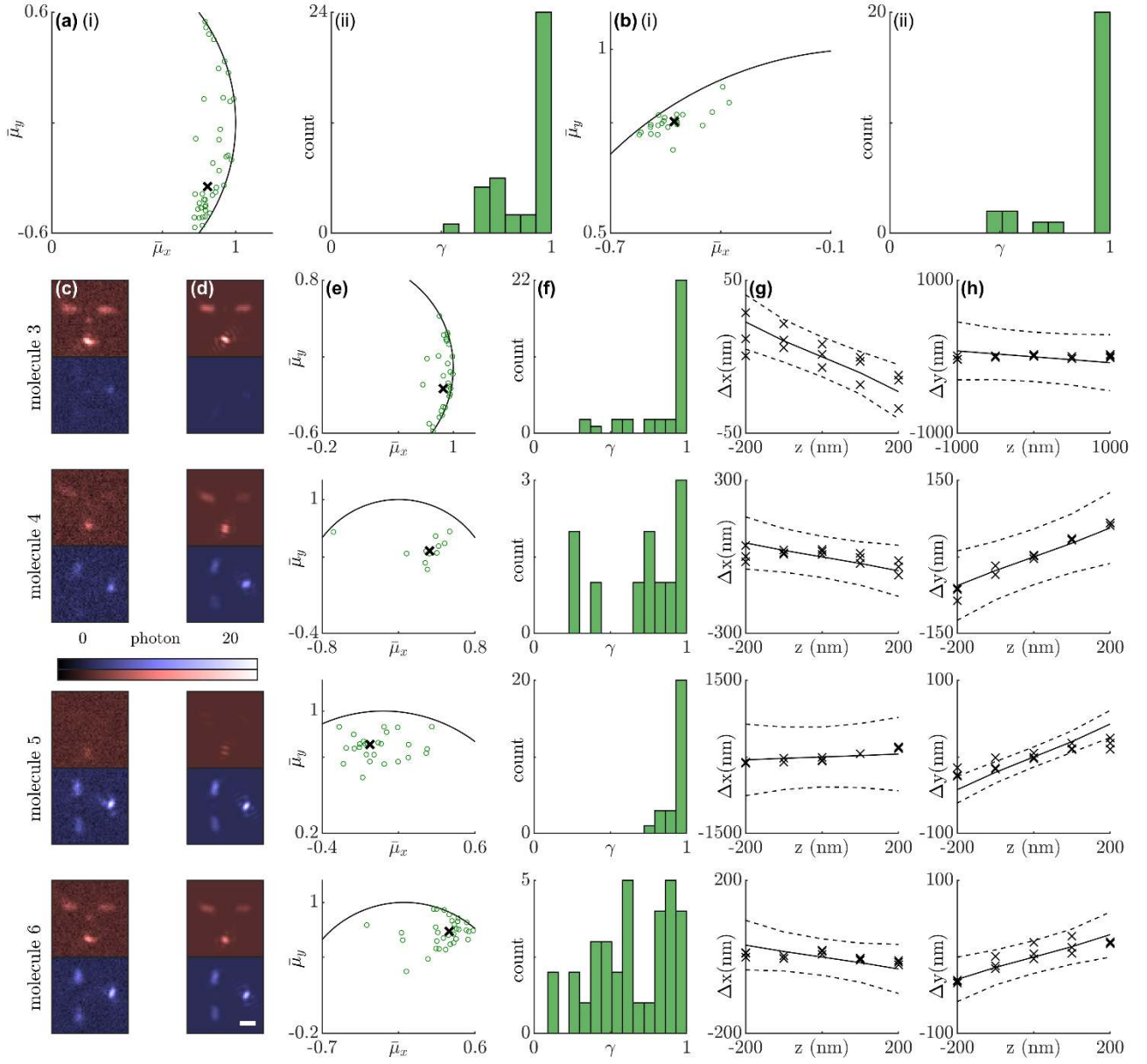


Figure S8. Orientation measurements of Atto 647N molecules. (i) The estimates of average orientation and (ii) rotational constraint of (a) molecule 1 and (b) molecule 2. For molecules 3-6, (c) raw images from the experiments visually match (d) the recovered images based on (e) the estimates of average orientation and (f) rotational constraint. Open circle represents each measurement and cross represents the median. Solid curve marks the orientation domain $\mu_x^2 + \mu_y^2 \leq 1$. Measured localization bias (cross) along (g) the x -axis in x -polarized channel and (h) the y -axis in y -polarized channel at different z positions. The solid line represents the predicted lateral translation from the Tri-spot's orientation measurement, and the dashed line marks the experimental localization precision (± 1 std. dev.). Scale bar: 1 μm ; Color bar: photons detected/pixel.

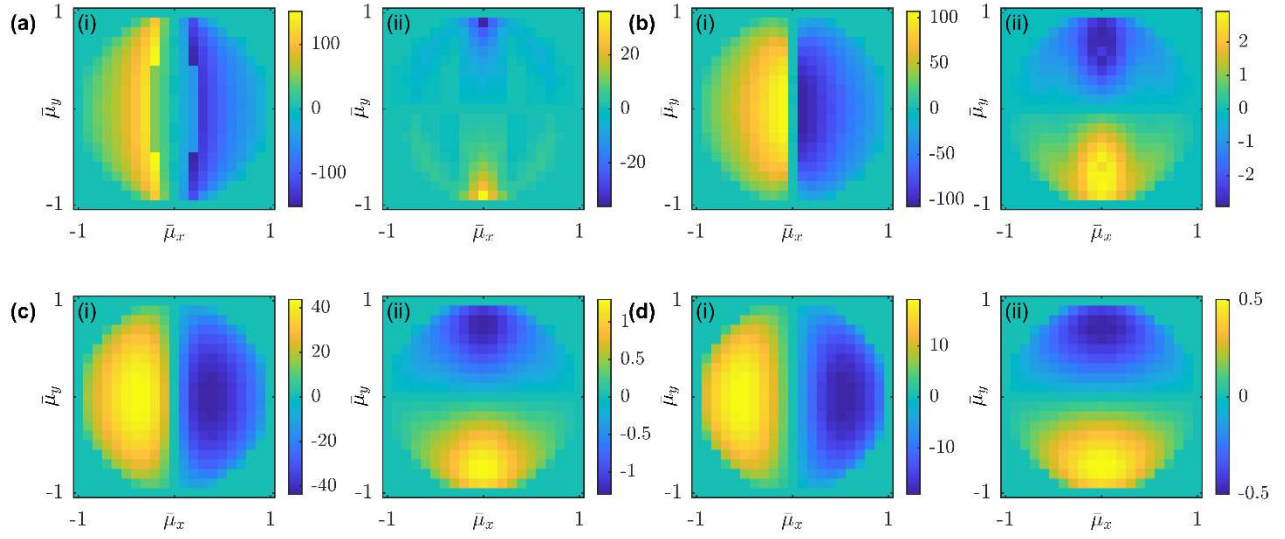


Figure S9. Localization bias, calculated using our image-formation model, in the x -polarized channel when a molecule is defocused by 200 nm with average orientation $\{\mu_x, \mu_y\} = [-1:0.1:1] \times [-1:0.1:1]$ and rotational constraint (a) $\gamma = 1$, (b) $\gamma = 0.75$, (c) $\gamma = 0.5$, and (d) $\gamma = 0.25$. (i) The localization bias along the x direction is larger than (ii) the bias along the y direction. For a fixed dipole emitter, the localization bias could be as much as 100 nm ((a-i), $\gamma = 1$), while the bias is reduced by 10 times for a less rotationally constrained emitter ((d-i), $\gamma = 0.25$). Color bar: nm.

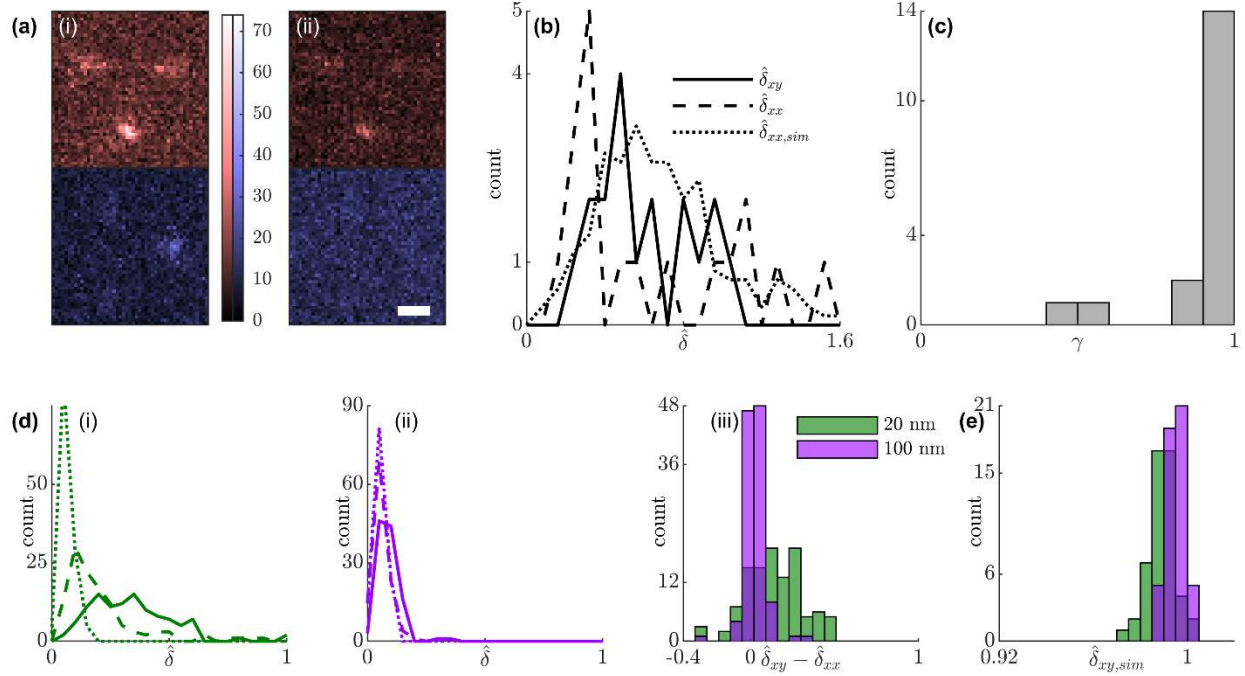


Figure S10. Emission anisotropy and rotation of the orientational second moments of fixed single molecules ($n=18$ molecules) under x - and y -polarized excitation. (a) Raw Tri-spot PSF images of single-molecule emitter pumped by (i) x -polarized and (ii) y -polarized light. (b) The measured distribution of the rotation of second-moment vectors between two x -pumped frames ($\hat{\delta}_{xx}$), and between one x -pumped and one y -pumped frame ($\hat{\delta}_{xy}$). Dotted line represents the distribution of $\hat{\delta}_{xx,sim}$ under SM SBR in simulations, dashed line represents the distribution of $\hat{\delta}_{xx}$ and solid line represents the distribution of $\hat{\delta}_{xy}$ in experiments. (c) Measured distribution of rotational constraint γ . (d) $\hat{\delta}_{xx}$ under x -polarized pumping and $\hat{\delta}_{xy}$ measured under x -polarized and y -polarized pump for each (i) 20-nm bead and (ii) 100-nm bead. (iii) The difference $\hat{\delta}_{xy} - \hat{\delta}_{xx}$ for 100-nm beads is smaller than that for 20-nm beads. (e) The measured distribution of the rotation of second-moment vectors between x - and y -polarized pump for simulated isotropic emitters (i.e. ensemble of independent fixed fluorescent molecules) at the fluorescent-bead SBR. Green, 20-nm beads; purple, 100-nm beads. Scale bar: 1 μm ; Color bar: photons detected/pixel.

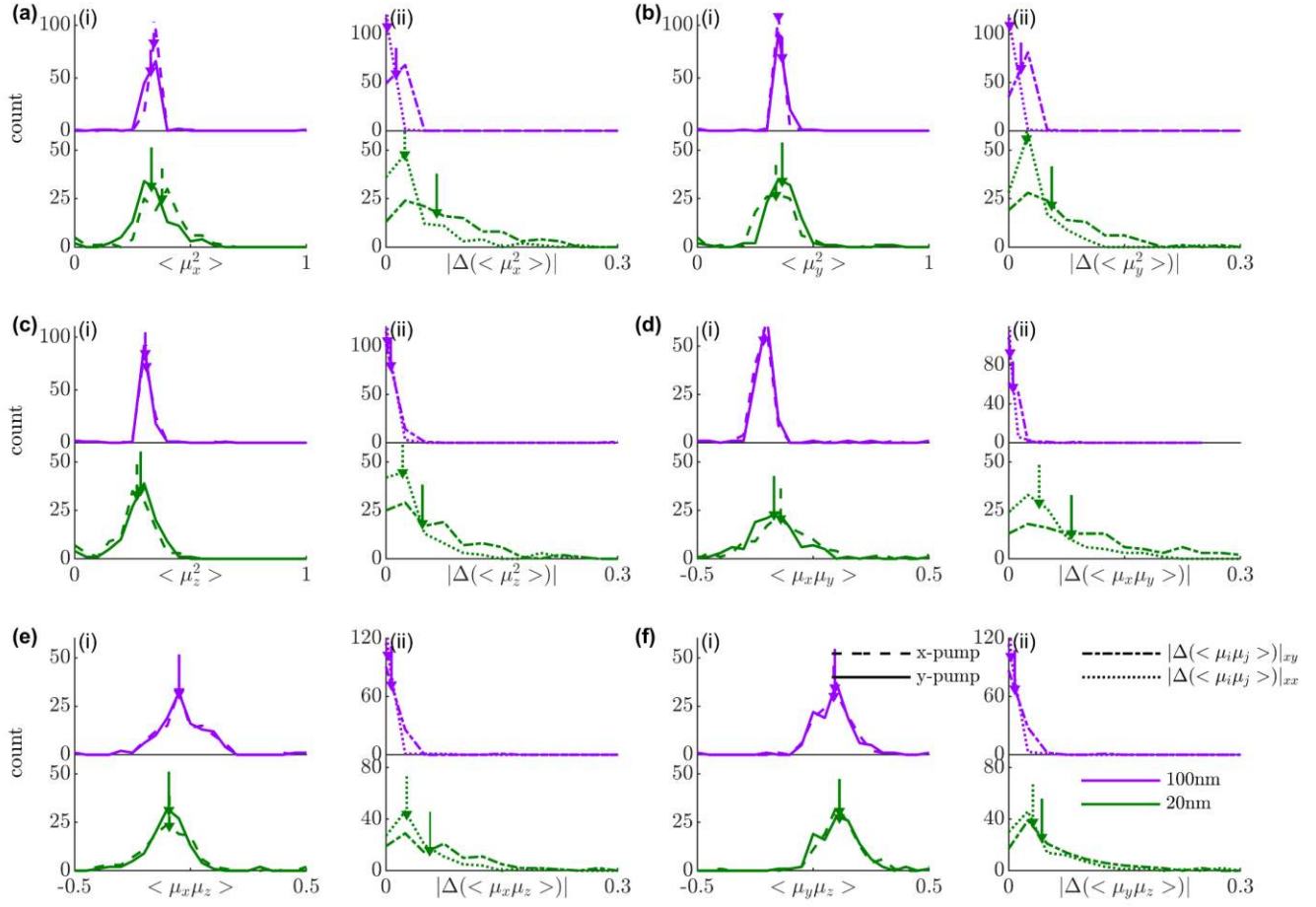


Figure S11. Distribution of second moments (a) $\langle \mu_x^2 \rangle$, (b) $\langle \mu_y^2 \rangle$, (c) $\langle \mu_z^2 \rangle$, (d) $\langle \mu_x \mu_y \rangle$, (e) $\langle \mu_x \mu_z \rangle$ and (f) $\langle \mu_y \mu_z \rangle$ of 20-nm beads and 100-nm beads under x -polarized and y -polarized excitation. Green, 20-nm beads; purple, 100-nm beads. (i) Population distribution of second moments. Dashed line represents the distribution of second moments measured under x -polarized light and solid line represents the distribution under y -polarized light. (ii) Difference in second moments under identical and orthogonal pumping polarizations computed for each bead. Dotted line represents the difference in second moments under constant x -polarized excitation and dash-dot line represents the difference in second moments between x -polarized and y -polarized excitation. Arrows represent the median of each distribution.

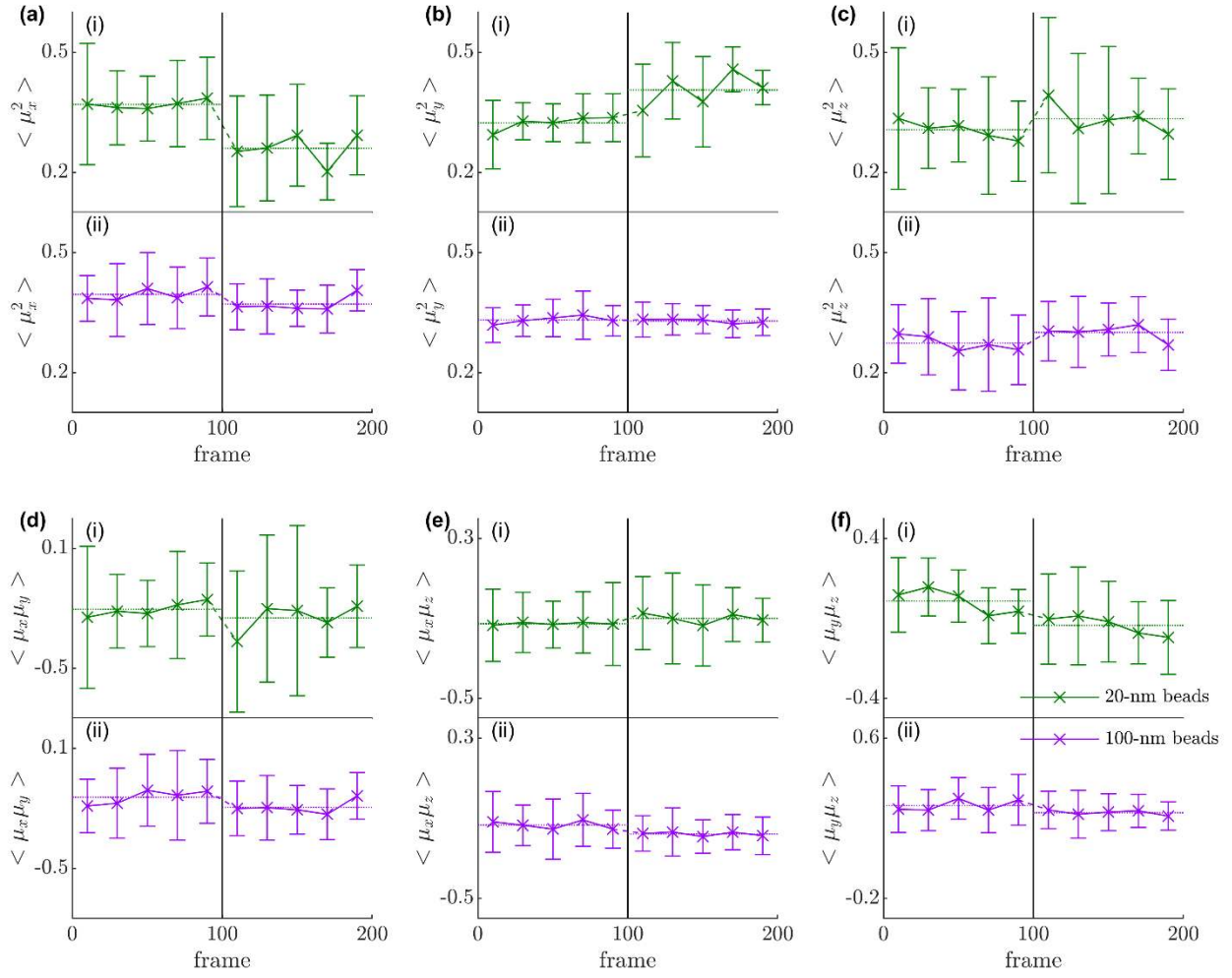


Figure S12. Measurements of orientational second moments (a) $\langle \mu_x^2 \rangle$, (b) $\langle \mu_y^2 \rangle$, (c) $\langle \mu_z^2 \rangle$, (d) $\langle \mu_x \mu_y \rangle$, (e) $\langle \mu_x \mu_z \rangle$ and (f) $\langle \mu_y \mu_z \rangle$ for the representative (i) 20-nm bead and (ii) 100-nm bead in Figure 2 over time. We calculate the average second moments every 20 frames. The first 100 frames are measured under x-polarized excitation, and the other 100 frames are measured under y-polarized excitation. Dotted lines represent the average second moments among 100 frames. Dashed lines and black vertical lines represent the excitation polarization change. Green, 20-nm beads; purple, 100-nm beads.

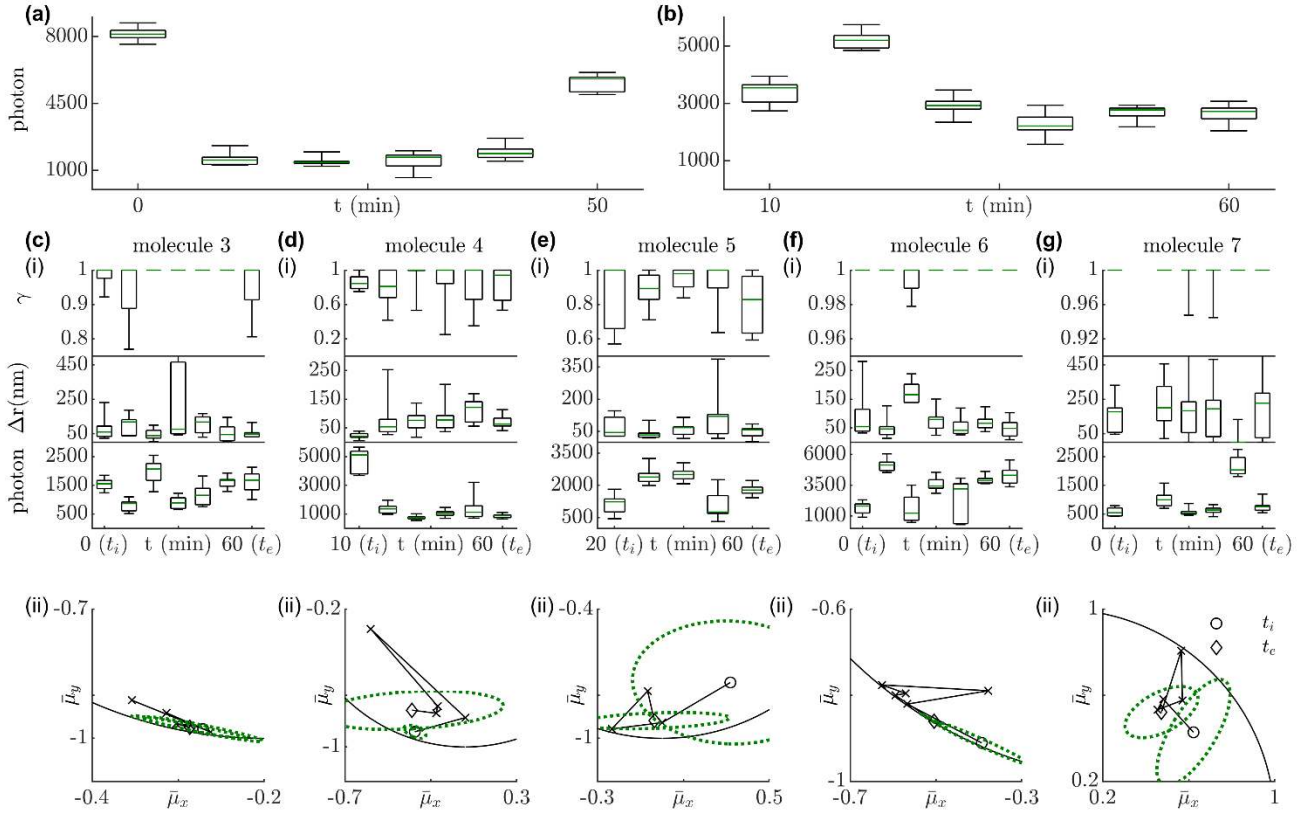


Figure S13. Rotational constraint, lateral diffusion, and orientation tracking of Atto 647N molecules embedded in a thin PVP film. Photons detected over time for (a) molecule 1 and (b) molecule 2 in Figure 3. (i) Rotational constraint γ , lateral displacement Δr , and photons detected over time for molecules (c) 3, (d) 4, (e) 5, (f) 6, and (g) 7. There is no correlation between photons detected and orientation parameters estimated, suggesting that the γ change is not due to the photon variation. t_i , time point at initial exposure to humid air; t_e , time point at end of experiment. Green: median; Box: first and third quartile; Error bar: minimum and maximum. (ii) Measured average orientation over time. Circle represents the beginning and diamond represents the end of the time-lapse measurement. Dashed green ellipse represents the covariance matrix in estimated orientation $(\bar{\mu}_x, \bar{\mu}_y)$ measured at the beginning and the end points and solid curve marks the orientation domain $\bar{\mu}_x^2 + \bar{\mu}_y^2 \leq 1$.

Table S1. Photon statistics and precision of orientation measurements

		average signal (photons/frame)	background (photons/ (pixel·frame))	precision (standard deviation)					
				$\bar{\mu}_x$	$\bar{\mu}_y$		γ		
Figures 1,S8	molecule 1	3795	21	0.06	0.34		0.13		
	molecule 2	2481	24	0.30	0.06		0.18		
	molecule 3	1507	13	0.09	0.35		0.22		
	molecule 4	1124	10	0.33	0.13		0.27		
	molecule 5	1361	11	0.20	0.08		0.08		
	molecule 6	1656	10	0.21	0.13		0.26		
Figures 3,S13				$\bar{\mu}_x(t_i)$	$\bar{\mu}_x(t_e)$	$\bar{\mu}_y(t_i)$	$\bar{\mu}_y(t_e)$	$\gamma(t_i)$	$\gamma(t_e)$
	molecule 1	2901	7	0.04	0.13	0.03	0.04	0.00*	0.05
	molecule 2	2936	6	0.02	0.03	0.02	0.02	0.00	0.00
	molecule 3	1273	6	0.12	0.12	0.02	0.02	0.03	0.07
	molecule 4	2258	7	0.05	0.45	0.03	0.10	0.09	0.18
	molecule 5	1803	7	0.39	0.30	0.24	0.03	0.18	0.16
	molecule 6	3485	6	0.09	0.03	0.04	0.02	0.00	0.00
	molecule 7	1032	4	0.15	0.14	0.21	0.10	0.00	0.00
Figure 2		-	-	γ (single frame)			γ (average among one-hundred frames)		
	20-nm beads	1041	1	0.31			0.03		
	100-nm beads	2217	1	0.18			0.02		

* Std. dev. measurements equal to zero for γ estimations are the result of calibration procedure (see Section 4.4 for details).

t_i , time point at initial exposure to humid air; t_e , time point at end of experiment.

References

- ¹ M. Böhmer and J. Enderlein, J. Opt. Soc. Am. B **20**, 554 (2003).
- ² M.A. Lieb, J.M. Zavislan, and L. Novotny, J. Opt. Soc. Am. B **21**, 1210 (2004).
- ³ D. Axelrod, J. Microsc. **247**, 147 (2012).
- ⁴ A.S. Backer and W.E. Moerner, J. Phys. Chem. B **118**, 8313 (2014).
- ⁵ A.S. Backer and W.E. Moerner, Opt. Express **23**, 4255 (2015).
- ⁶ S. Stallinga, J. Opt. Soc. Am. A **32**, 213 (2015).
- ⁷ A.S. Backer, M.P. Backlund, A.R. von Diezmann, S.J. Sahl, and W.E. Moerner, Appl. Phys. Lett. **104**, 193701 (2014).
- ⁸ A.S. Backer, M.P. Backlund, M.D. Lew, and W.E. Moerner, Opt. Lett. **38**, 1521 (2013).
- ⁹ N. Di Fiori and A. Meller, Biophys. J. **98**, 2265 (2010).
- ¹⁰ S. Sharma, K. Chakraborty, B.K. Müller, N. Astola, Y.-C. Tang, D.C. Lamb, M. Hayer-Hartl, and F.U. Hartl, Cell **133**, 142 (2008).
- ¹¹ K. Kolmakov, V.N. Belov, J. Bierwagen, C. Ringemann, V. Müller, C. Eggeling, and S.W. Hell, Chem. - A Eur. J. **16**, 158 (2010).
- ¹² T. Niehörster, A. Löschberger, I. Gregor, B. Krämer, H.J. Rahn, M. Patting, F. Koberling, J. Enderlein, and M. Sauer, Nat. Methods **13**, 257 (2016).